

Journal Pre-proofs

Exploring the importance of authigenic clay formation in the global Li cycle

Elizabeth Andrews, Philip A. E. Pogge von Strandmann, Matthew S. Fantle

PII: S0016-7037(20)30525-1
DOI: <https://doi.org/10.1016/j.gca.2020.08.018>
Reference: GCA 11890

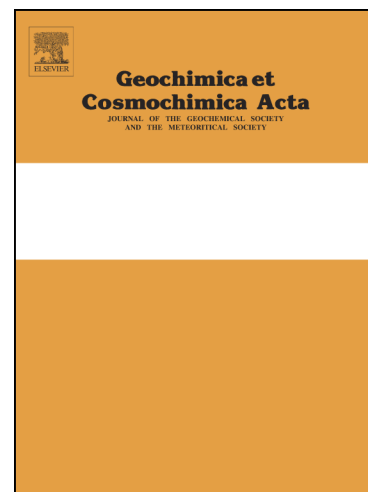
To appear in: *Geochimica et Cosmochimica Acta*

Received Date: 20 December 2019
Revised Date: 15 August 2020
Accepted Date: 17 August 2020

Please cite this article as: Andrews, E., A. E. Pogge von Strandmann, P., Fantle, M.S., Exploring the importance of authigenic clay formation in the global Li cycle, *Geochimica et Cosmochimica Acta* (2020), doi: <https://doi.org/10.1016/j.gca.2020.08.018>

This is a PDF file of an article that has undergone enhancements after acceptance, such as the addition of a cover page and metadata, and formatting for readability, but it is not yet the definitive version of record. This version will undergo additional copyediting, typesetting and review before it is published in its final form, but we are providing this version to give early visibility of the article. Please note that, during the production process, errors may be discovered which could affect the content, and all legal disclaimers that apply to the journal pertain.

© 2020 Elsevier Ltd. All rights reserved.



Exploring the importance of authigenic clay formation in the global Li cycle

Elizabeth Andrews^{1,2,*}, Philip A. E. Pogge von Strandmann³, and Matthew S. Fantle¹

1 – Dept. of Geosciences, The Pennsylvania State University, University Park, PA 16802

2 – Hydrologic Science and Engineering, Dept. of Geology and Geological Engineering, Colorado School of Mines, Golden, CO 80401

3 – London Geochemistry and Isotope Centre (LOGIC), Institute of Earth and Planetary Sciences, University College London and Birkbeck, University of London, Gower Place, London, WC1E 6BS, UK

* Corresponding author: eandrews1@mines.edu, Tel: +1 484-767-0593

Keywords: global Li cycle; Li isotopes; reactive transport modeling; clay authigenesis; geochemical proxies; carbonate-rich marine sediments

1 Abstract

2 Lithium isotopic ($\delta^7\text{Li}$) and elemental concentrations in pore fluids and carbonates from IODP
3 Site U1338 Hole A (eastern equatorial Pacific Ocean) suggest that clay authigenesis (i.e., *in situ*
4 precipitation) is a significant sink for Li in carbonate-rich sedimentary sections. Systematic
5 variations in pore fluid $\delta^7\text{Li}$ with depth in the section suggest that clay authigenesis can (i)
6 strongly decrease pore fluid Li concentrations with depth and (ii) fractionate Li isotopically to a
7 considerable degree ($\Delta \sim 5$ to 21‰ relative to seawater). We hypothesize that clay authigenesis
8 in carbonate-rich sections occurs in the presence of reactive biogenic silica, and reactive
9 transport modeling supports the contention that the pore fluid $\delta^7\text{Li}$ depth profile at Site U1338 is
10 best explained by faster authigenesis at depth. The significance of clay authigenesis in carbonate-
11 rich sediments is two-fold: if global in scale, (i) it can generate sizeable output fluxes in the
12 global Li cycle, and (ii) the evolution of the sedimentary system over time can markedly impact
13 the isotopic composition of the global Li output flux. We compile ODP and IODP pore fluid Li
14 data from 267 sites; of these, 207 have Li pore fluid concentration gradients in the upper 50-100
15 meters that indicate the sites as diffusive sinks of Li. We then estimate that clay authigenesis in
16 carbonate-rich sediments could reasonably generate a Li output flux on the order of $\sim 1.2 \cdot 10^{10}$
17 moles/year, which is comparable to the gross input fluxes in the modern Li cycle. A series of
18 reactive transport simulations illustrate how clay authigenesis might impact the isotopic
19 composition of the output flux of Li from the global ocean. The suggestion is that applying a
20 constant fractionation factor from the global ocean over time is likely incorrect, and that secular
21 changes in the $\delta^7\text{Li}$ of the output flux will be driven by rates of authigenesis, burial rates, and the
22 depth extent of authigenesis in the sedimentary section. Utilizing a time-dependent, depositional
23 diagenetic model, the $\delta^7\text{Li}$ values of bulk carbonate are shown to be a consequence not of
24 recrystallization alone, but recrystallization in the presence of clay authigenesis. Further, our
25 model results are used to illustrate how carbonate $\delta^7\text{Li}$ may be used to constrain the temporal
26 evolution of clay authigenesis in the sedimentary section. Ultimately, this work suggests that the
27 Li isotopic composition of bulk carbonates can be altered diagenetically. However, such
28 alteration is not a detriment, but provides useful information on those diagenetic processes in the
29 sedimentary column that impact the global Li cycle. Thus, Li isotopes in bulk carbonates have
30 the potential to elucidate diagenetic controls on the global Li cycle over long time scales.

31

32 1. Introduction

33 The desire to reconstruct carbon cycling and climate variability over geologic time scales
34 has spurred development of novel isotopic proxies that can constrain processes within the carbon
35 cycle, such as silicate weathering, that act as feedbacks on atmospheric CO_2 concentrations over
36 geologic time scales. Lithium (Li) isotopes have been proposed as proxies for present and past
37 continental silicate weathering (Millot et al., 2010; Pogge von Strandmann et al., 2013; Dellinger
38 et al., 2014; Dellinger et al., 2017), and, accordingly, have been measured in both carbonate and

39 siliciclastic sediments in order to quantify the intensity of continental weathering over geologic
40 time scales (e.g., Misra and Froelich, 2012; Pogge von Strandmann et al., 2017). The Li isotopic
41 composition of seawater is impacted by silicate rock weathering but is much less sensitive to
42 carbonate rock weathering (Kisakurek et al., 2005), which is the basis for the proposal that Li
43 isotopes are ideal tools for reconstructing the secular evolution of silicate weathering processes.
44 One approach that has been used quite successfully is to utilize carbonate minerals (such as
45 foraminiferal tests) as proxy archives to reconstruct the $\delta^7\text{Li}$ of seawater, and then interpret this
46 signal in terms of the silicate weathering input to the ocean over geologic time scales (Misra and
47 Froelich, 2012; Pogge von Strandmann et al., 2013; Lechler et al., 2015). Carbonate is a
48 reasonable archive because while the Li isotopic composition of foraminiferal tests can be
49 species specific, they appear to closely reflect the $\delta^7\text{Li}$ of the water in which they grew (Hall et
50 al., 2005; Hathorne and James, 2006; Vigier et al., 2007; Dellinger et al., 2018). It is also worth
51 noting that one assumption that is made when interpreting the putative seawater $\delta^7\text{Li}$ record is
52 that secular variability in seawater $\delta^7\text{Li}$ is driven almost entirely by variations in the riverine
53 input flux.

54 Before reconstructing secular trends in silicate weathering using any proxy archive, be it
55 siliciclastic or carbonate, it is crucial to consider the effect of post-depositional (or post-
56 formational) alteration of the archive (i.e., diagenesis). Bulk carbonates have been shown to react
57 and recrystallize relatively rapidly (Fantle and DePaolo, 2007; Fantle, 2015; Gorski and Fantle,
58 2017; Huber et al., 2017), impacting strontium, oxygen, and magnesium isotope compositions
59 and Mg/Ca ratios (Richter and DePaolo, 1987; Schrag et al., 1992; Fantle and DePaolo, 2006;
60 Chanda and Fantle, 2017). In contrast to elements such as Ca and Sr, and similar to Mg, Li has a
61 low concentration in carbonates (1-2 ppm; Hoefs and Sywall, 1997; Burton and Vigier, 2012)

62 compared to its concentration in siliciclastics (50-500 ppm; Hein et al., 1979; Zhang et al., 1998).
63 Likewise, siliciclastic sediments have also been inferred to be reactive: biogenic silica has been
64 proposed to react in the sedimentary column to form authigenic clays (Michalopoulos and Aller,
65 1995; Michalopoulos et al., 2000; Michalopoulos and Aller, 2004), while amorphous silica has
66 been shown to react even over short, laboratory time scales (Geilert et al., 2014; Roerdink et al.,
67 2015; Fernandez et al., 2019).

68 Despite the clear evidence for mineral reaction in the sedimentary column, there has been
69 a limited amount of work on the impact of diagenesis on the Li isotopic composition of proxy
70 archives (You et al., 2003; Ullmann et al., 2013; Dellinger et al., 2020). While carbonate
71 recrystallization has been the focus of Li-based diagenetic studies to date, authigenic clay
72 formation, in particular, has the potential to impact carbonate archives in a range of ways. First,
73 carbonate-hosted Li is susceptible to contamination by relatively small amounts of siliciclastic
74 material (e.g., authigenic clays) that may be intimately associated with carbonate minerals and/or
75 fossils. Second, authigenic clay formation at depths in the sedimentary column that are out of
76 diffusive communication with the overlying seawater reservoir can shift pore fluid $\delta^7\text{Li}$ to
77 markedly higher values than seawater, which increases the isotopic leverage to alter via
78 recrystallization (Zhang et al., 1998; Pistiner and Henderson, 2003; Chan et al., 2006; Vigier et
79 al., 2008; Wimpenny et al., 2015; Hindshaw et al., 2019; Pogge von Strandmann et al., 2019a;
80 Fantle et al., 2020). It remains to be seen, however, whether or not clay authigenesis is important
81 in carbonate-rich sediments.

82 If clay authigenesis is significant in carbonate-rich sediments, then there is potential for
83 this diagenetic process to impact the global Li cycle to a considerable extent. While the question
84 of whether marine sediments are marine Li sources or sinks has been debated for decades

85 (Stoffyn-Egli and Mackenzie, 1984; Huh et al., 1998; Misra and Froelich, 2012), the focus has
86 mainly been on siliciclastic, and not carbonate-rich, sections. Prevailing wisdom holds that the
87 balance between dissolution and precipitation of Li-containing silicates in marine sedimentary
88 systems dictates whether a given sedimentary section is a Li source or sink (Stoffyn-Egli and
89 Mackenzie, 1984). Because biogenic carbonates have very low Li concentrations, there is
90 considerable potential to develop strong diffusive gradients, and thus large output fluxes, in
91 carbonate-rich sections. Further, there is potential for such output fluxes to evolve elementally
92 and isotopically over time. Ultimately, then, identifying the spatial extent of authigenesis in the
93 sedimentary column, quantifying its impact on the global Li cycle, and elucidating its evolution
94 over time is critical, as this sink plays an important role in balancing hydrothermal, riverine, and
95 subduction reflux inputs over geologic time scales (Hathorne and James, 2006; Misra and
96 Froelich, 2012).

97 If we are to use Li isotopes in carbonate-rich sediments to peer into the past confidently
98 and unambiguously, we must understand the systematics of authigenesis. Amongst the questions
99 that must be addressed in order to build that confidence are:

- 100 (1) Does authigenic clay formation impact the Li isotopic composition of carbonate proxy
101 archives?
- 102 (2) Does carbonate recrystallization incorporate the signal of pore fluid whose chemistry is
103 impacted by clay authigenesis?
- 104 (3) Are sizeable fluxes in the global Li cycle associated with carbonate-rich sites? If so, what
105 is the isotopic fractionation associated with such fluxes and does this evolve over time?

106 With these questions in mind, the objective of the current study is to investigate the impact
107 of diagenesis on the Li isotopic composition of bulk carbonates in a carbonate-rich section in the
108 eastern equatorial Pacific (IODP Leg 321, Site U1338, Hole A; 2°30.469'N, 117°58.178'W). This

109 site was chosen because there is a significant pore fluid Li concentration gradient in the
110 sedimentary column that presumably represents the balance between diffusion of Li into the
111 sediment and removal from pore fluids by reaction in the sedimentary column. We analyzed the
112 elemental and isotopic composition of Li in a suite of pore fluids from Site U1338, as well as
113 sequentially leached bulk carbonates. Selected sediments were imaged using scanning electron
114 microscopy (SEM) and energy dispersive spectroscopy (EDS) to determine qualitative spatial
115 trends in the chemistry of particles sampled from the sedimentary column, while mineralogy was
116 constrained by powder X-ray diffraction (XRD). Multicomponent reactive transport modeling
117 was conducted in order to constrain the balance between clay authigenesis and biogenic silica
118 dissolution at Site U1338; a diffusion experiment was also performed to help constrain the
119 fractionation factor associated with diffusion, given the dearth of existing constraints. The
120 constraints provided by the modeling are then utilized to discuss the global relevance of clay
121 authigenesis in carbonate-rich sections.

122 Ultimately, our analysis suggests that authigenic clay formation (i) occurs in carbonate-rich
123 sections, (ii) controls the Li isotopic composition of pore fluids, and (iii) has the potential to
124 impact the Li isotopic composition of bulk carbonates. Clay authigenesis could account for as
125 much as a $\sim 1.2 \cdot 10^{10}$ mol Li/ year output flux in the global Li cycle, which is similar in
126 magnitude to the marine authigenic clay flux constrained by Hathorne and James (2006) and
127 Misra and Froehlich (2012). Interestingly, this flux has the potential to vary temporally in both
128 mass flux and isotopic composition, which could help explain the evolution of seawater $\delta^7\text{Li}$
129 over million-year time scales.

130

131

132 2. Site Description

133 Site U1338 was drilled in 2009 during IODP Expedition 320/321, the goal of which was
134 to collect an age transect of Cenozoic sediments deposited at the paleo-position of the equator
135 across the eastern equatorial Pacific Ocean (see Figure 1 for location of drill sites). The oldest
136 site (U1331) sits on 53 Ma basaltic basement, while the youngest site (Site U1338) sits
137 conformably on 18 Ma basement. Four holes were drilled at Site U1338 (A, B, C, and D); in this
138 study, we focus on Hole A. The water depth at Site U1338, Hole A is ~4205 meters and drilling
139 penetrated 410 meters in the sedimentary column, which is comprised primarily of nannofossil
140 ooze, with varying amounts of foraminifers and biogenic silica (Palike et al., 2010b).

141 Stratigraphically, the sediment column contains three distinct lithostratigraphic units (Fig.
142 1b). Unit I (from 0 to 50 meters below seafloor, mbsf) consists of Pleistocene to mid-Pliocene
143 sediment, which is primarily white, brown, and gray nannofossil ooze containing variable
144 amounts of diatoms and radiolaria (Palike et al., 2010b). The second unit, Unit II, encompasses
145 the upper Miocene to the mid-Pliocene between 50.35 and 243.94 mbsf, and consists of light
146 green and light gray nannofossil ooze with dark, diatom-rich intervals. Mottling/color changes in
147 this unit likely represent variations in redox state (Palike et al., 2010b). The final sedimentary
148 unit, Unit III, is lower to upper Miocene in age and spans 243.94 to 408.37 mbsf. Unit III
149 consists of white, pale yellow, light greenish gray, and very pale brown nannofossil oozes and
150 chalks. In Unit III, there are darker green and gray intervals that contain more siliceous
151 microfossils. Unit III conformably overlies the 18 Ma basaltic basement (Palike et al., 2010b).
152 On the revised method composite depth (rmcd) scale, which allows for comparisons between
153 sites, the unit intervals are 0 to 55.91 rmcd for Unit I, 55.91 to 271.72 rmcd for Unit II, and
154 271.72 to 453.43 rmcd for Unit III (the rmcd scale will be used throughout this paper).

155 Porosity at Site U1338, Hole A decreases with depth, from ~80% at the sediment-water
156 interface to ~50% near the sediment-basement interface (Fig. 1c). Carbonate content varies
157 between ~26 and ~91 wt. %, while SiO₂ content ranges from ~5 to 53 wt. % (Fig. 1d and 1e). In
158 the upper 250 meters, the CaCO₃ content is high but variable, ranging from 26 to 88 wt. %, while
159 the SiO₂ content ranges between ~10 and 40 wt. % (Palike et al., 2010b). Below 250 meters, the
160 variability in the solid phase CaCO₃ content decreases, ranging between 66 and 91 wt. %; the
161 solid phase SiO₂ content in this interval varies between 10 and 20 wt. %. Several measurements
162 of temperature were made during drilling: at the sediment-water interface, the temperature was
163 ~1.6°C, and increased with depth from 3.3°C at ~41 mcd to 12.7°C at ~325 mcd (Fig. 1g)
164 (Palike et al., 2010b).

165 Major and trace elements were analyzed in the squeeze-cake pore fluids during the cruise
166 by inductively-coupled plasma atomic emission spectroscopy (ICP-AES) (Palike et al., 2010a).
167 The most notable geochemical trend with depth is the pore fluid Li concentration, which
168 decreases strongly with depth from the seawater value (26 μM) to a minimum of ~2 μM at 250
169 meters, before increasing again to seawater concentration (26 μM) near the sediment-basement
170 interface (Fig. 2a). The increase in Li concentration at the sediment-basement interface has been
171 inferred to be the result of advective seawater flow through the basement (Palike et al., 2010b).
172 The pore fluid Sr concentration profile is also significant, increasing with depth to a maximum of
173 ~400 μM at ~240 meters before decreasing with depth to seawater values (~90 μM) (Fig. 2b).
174 The increase in Sr concentration with depth likely represents dissolution and/or recrystallization
175 of biogenic carbonate (Palike et al., 2010b). Estimates of recrystallization extent are ~20% at 18
176 Ma (Voigt et al., 2015).

177 Pore fluid silicic acid concentrations increase linearly with depth and stabilize at ~1200
178 μM until just above the sediment-basement interface. It has been suggested that the dissolution
179 of biogenic silica causes the increase in silicic acid concentrations (Palike et al., 2010b) (Fig. 2c).
180 The alkalinity depth trend is similar to that of silicic acid; alkalinity increases from 2.7 mM at the
181 sediment-water interface to 4.2 at ~150 meters. Below 150 mcd, the alkalinity becomes more
182 variable, but the general trend is a decrease with depth towards 2.8 mM at the sediment-
183 basement interface (Fig. 2h). The pH ranges from 7.4 to 7.7, decreasing slightly over the upper
184 250 meters and increasing to ~7.6 at the sediment-basement interface (Fig. 2d). Dissolved Mg,
185 Ca, and sulfate decrease slightly in the uppermost 200 meters of the section. Below 200 mcd,
186 the Mg and SO_4^{2-} concentrations remain relatively constant while Ca concentrations increase
187 slightly (Fig. 2e,f,g).

188

189 3. Methods

190 3.1 Analytical Techniques

191 The pore fluids were collected through whole-round squeezing completed on the Joides
192 Resolution. Upon arrival at Penn State, the pore fluids were filtered through an acid-washed 0.2
193 μm PVDF (polyvinylidene fluoride) syringe filter. Samples were then digested using perchloric
194 acid (HClO_4) and hydrofluoric acid (HF) to remove organics and dissolved silica. A small
195 aliquot of each sample (pre-digestion) was analyzed on ICP-AES and ICP-MS (inductively
196 coupled plasma atomic emission spectroscopy and mass spectrometry) to determine the
197 concentration of major and trace elements, including Li, in the pore fluid. The total charge
198 equivalent of the sample was calculated along with the Li concentration to determine the amount
199 of sample to be loaded on an ion exchange column for separation of Li from the matrix.

200 To obtain a sufficient amount of Li for isotopic analysis, 1 g of sediment sample was
201 sequentially extracted following a slightly modified Tessier extraction designed to dissolve bulk
202 carbonates for trace metal analysis (Apitz, 1991; Delaney and Linn, 1993). Bulk sediments were
203 first treated with 50 mL of 1 N ammonium hydroxide (NH_4OH) to release Li (and other cations)
204 bound to exchange sites. The samples were subsequently rinsed with 18.2 M Ω deionized water
205 (MQ water) buffered to pH 10 with NH_4OH . Carbonates were then dissolved in 1 N acetic acid
206 for 5 hours and centrifuged; the supernatant was decanted and saved. This acetic acid leach was
207 not buffered with sodium acetate as described in the original extraction method to avoid adding
208 additional cations (such as Na^+) to the solution. The carbonate extraction was filtered through a
209 0.2 μm PVDF filter and analyzed for Li using a X-Series II quadrupole ICP-MS in the
210 Laboratory for Isotopes and Metals in the environment (LIME). The residual solid (silicates and
211 biogenic silica) was then digested using a mixture of concentrated HNO_3 , HCl , HClO_4 , and HF .
212 Upon complete dissolution of the solid, the solution was then analyzed for cations by Perkin-
213 Elmer 5300 Optima 5300DV ICP-AES and for Li by ICP-MS. The errors associated with
214 concentration measurements are approximately 2%, as determined by repeated analysis of in-
215 house laboratory standards.

216 The mineralogy of the non-carbonate fraction of the sediment was determined by powder
217 X-ray diffraction. Prior to analysis, the samples were treated with 1 N acetic acid to remove
218 carbonate so that the trace phases in the sediment could be identified. Samples were then rinsed
219 with MQ water and wet sieved. The $< 63 \mu\text{m}$ size fraction was dried at 30°C and analyzed. A
220 PANalytical X'Pert Pro MPD X-ray Diffractometer with a copper tube and an X-ray wavelength
221 (K_α) of 1.541874 \AA was used for the analysis. Scanning occurred for a total of 17 minutes and
222 ranged from 5° to $70^\circ 2\theta$.

223 Electron microscope images of the samples were taken using a FEI Nova NanoSEM 630
224 Scanning Electron Microscope at the Materials Research Institute (MRI) at Penn State. Samples
225 were wet sieved with water, allowed to air dry, and the $>63\ \mu\text{m}$ fraction was attached by carbon
226 tape to an aluminum stub. The stubs were coated with 5 nm of iridium to minimize sample
227 charging and permit qualitative elemental analysis using standard-less energy dispersive
228 spectroscopy (EDS). Scanning electron images were typically taken at a working distance of 3
229 mm, a voltage of 5 to 10 keV, and a spot size of 3.0 nm. EDS data, which were used to assess the
230 chemical composition of the sediments, were collected at 10 keV and a spot size of ~ 6.0 nm.
231 Scans were collected for 2 minutes and the data analyzed, and elemental maps generated, using
232 Aztec EDS software.

233 Prior to isotopic analysis, Li in pore fluids and the residual fraction of the sediments was
234 purified chromatographically using AG-50Wx12 200-400 mesh resin in polypropylene Bio-Rad
235 columns. The bed volume of the column is 2 mL and the column has an 8 mL reservoir volume.
236 The resin was pre-washed in batches with 4 N HCl and 4 N HNO₃. The columns were loaded to
237 2 mL, which was approximately 8 cm in height. The resin was washed again in column with 4 N
238 HCl and 4 N HNO₃ and then conditioned with 0.2 N HCl. Samples were loaded onto the column
239 in ~ 0.2 mL of 0.2 N HCl. Elution of Li was carried out with ~ 30 mL of 0.2 N HCl, then the
240 matrix was cleaned out of the column with 4 N HCl. The procedural blank was less than 0.8 ng
241 of Li. No Li was detected in the procedural blank on the ICP-MS where the detection limit was
242 0.1 ng/g in an 8 mL sample. The Li cut and the post cut were both analyzed by ICP-MS to
243 calculate column yields (ranged between 98 and 104%), as incomplete recovery can cause
244 significant fractionation (Tomascak et al., 2016). To ensure good yields, the total mass loaded
245 onto the column was limited to $<7.5\%$ of the cation exchange capacity (c.e.c.) of the column. In

246 samples with low Li:Na ratios, the sample was purified on multiple columns in parallel in order
 247 to maintain this cutoff. Samples were dried down and resuspended in 2% HNO₃ to ~30 ppb prior
 248 to analysis on the ThermoFisher Scientific Neptune Plus MC-ICP-MS in the Metal Isotope
 249 Laboratory (MIL) at Penn State.

250 Isotopic analysis was conducted on pore fluid and residual fraction samples and standards
 251 that had a Li concentration of ~30 ppb. Sample-standard bracketing was utilized, in which
 252 reagent blanks (BLK) were also measured (i.e., in the sequence: BLK-STD-BLK-SAMP-BLK-
 253 STD-BLK); the measured blank was corrected for by averaging the bracketing blank ratios and
 254 subtracting that value from the measured standard and sample values (see Eqn. S2 in
 255 Supplemental Information for details). The bracketing standard used was IRMM-016, which is
 256 isotopically similar to L-SVEC ($\Delta^7\text{Li}_{\text{IRMM-016-L-SVEC}} = -0.2 \pm 0.3\text{‰}$, Tomascak et al., 2016), and all
 257 delta values are reported relative to this standard. The notation for isotopic measurements is:

$$258 \quad \delta^7\text{Li} = ((^7\text{Li}/^6\text{Li})_{\text{sample}} / (^7\text{Li}/^6\text{Li})_{\text{IRMM-016}} - 1) \cdot 10^3 \quad [1]$$

259 where the standard ratio represents the average of the bracketing standard measured before and
 260 after the sample and blank. Repeated analysis of international standards were in agreement with
 261 literature values: analysis of IAPSO yielded $\delta^7\text{Li} = 31.2 \pm 0.9$ and analysis of BCR-1 yielded
 262 $\delta^7\text{Li} = 2.8 \pm 0.7\text{‰}$ (in agreement with Magna et al., 2004 and Rudnick et al., 2004). All reported
 263 errors are 1 standard deviation.

264 The carbonate and exchangeable fractions of the leaches were chromatographically
 265 separated and analyzed in the London Geochemistry and Isotope Centre (LOGIC). Sufficient
 266 leachate was evaporated to attain ~5ng of Li, and passed through a two-stage cation exchange
 267 column procedure (AG50W X-12), eluting with dilute HCl (Pogge von Strandmann et al., 2011).

268 Column splits collected before and after the main elute, and analyzed for Li contents, show that
269 for each sample >99.9% of the sample was collected for isotopic analysis.

270 Purified carbonate and exchangeable leach samples with a concentration of 5 ppb were
271 analyzed on a Nu Plasma 3 MC-ICP-MS, using a sample-standard bracketing procedure relative
272 to IRMM-016. Each sample was measured three separate times during each analytical procedure,
273 repeat measurements being separated by several hours (but during the same analytical session).
274 We present the two standard deviation of these three repeats as the internal uncertainty on each
275 sample. Subsequent to analysis, sample $\delta^7\text{Li}$ was renormalized to the LSVEC standard, as
276 detailed in Pogge von Strandmann et al. (2019). The results of different international rock and
277 solution standards analyzed by this method are detailed in Pogge von Strandmann et al., 2011,
278 2019. Seawater analyzed during these particular analytical runs yielded $\delta^7\text{Li} = 31.4 \pm 0.2$ and
279 $31.2 \pm 0.2\%$.

280

281 *3.2 Multicomponent Reactive Transport Modeling*

282 Multicomponent reactive transport modeling was conducted using CrunchTope, a
283 reactive transport code that incorporates isotopes (see Druhan and Maher, 2014; Steefel et al.,
284 2014; Steefel et al., 2015 for governing equations and Supplemental Information for example of
285 input file blocks detailing initial and boundary conditions, as well as transport parameters).
286 Briefly, CrunchTope uses the advection dispersion equation to calculate transport; mineral
287 dissolution and precipitation are governed by kinetic rate laws following Transition State
288 Theory. Variability in the isotopic composition of model pore fluids can be generated by (i)
289 differences in the rate constants for nuclide-specific precipitation reactions ($\alpha_{\text{clay-fluid}} \approx 0.986$ -

290 0.990; Pistiner and Henderson, 2003; Vigier et al., 2008), (ii) distinct stoichiometries of
291 dissolving minerals (i.e., biogenic silica), and/or (iii) differences in the diffusion coefficients for
292 ${}^6\text{Li}^+(\text{aq})$ and ${}^7\text{Li}^+(\text{aq})$ (see below). The objectives of the modeling were to estimate the rate of
293 clay authigenesis that would explain the Li isotopic and elemental pore fluid data, predict the
294 volume of secondary clays this process would produce, and to investigate various scenarios with
295 respect to reactivity within the sedimentary column. The model domain was a one-dimensional
296 column containing 460 nodes spaced at 1 m (i.e., representative of Site U1338). Dirichlet
297 conditions were set at the upper and lower boundaries of the domain, which permitted transport
298 fluxes across both boundaries. No lateral flow was allowed.

299 The measured sediment lithology at Site U1338 constrained the initial conditions
300 assumed in all Site U1338-specific reactive transport models. The initial model solid phase, for
301 instance, was constrained by the average geochemistry (e.g., CaCO_3 and SiO_2 weight percent,
302 porosity, etc.) of the previously described lithologic units (Units I and II are combined, while
303 Unit III is considered a separate zone). Initial pore fluid Li concentration and isotopic
304 composition is assumed to be the same as modern seawater ($m_{\text{Li}^+} = 26 \mu\text{M}$; $\delta^7\text{Li} = 31.5\text{‰}$).
305 Model porosities are set to 0.75 for Units I and II and 0.63 for Unit III, reflecting the average
306 measured porosity of each unit. The temperature in the model was assumed to be a uniform
307 10°C , unless otherwise noted; the temperature determined the diffusion coefficients defined in
308 the TRANSPORT block of the input file (see SI for details).

309 Burial can be applied in CrunchTope such that material is added to the top of the section,
310 though CrunchTope does not do compaction and thus maintains a constant sedimentary column
311 thickness. Therefore, if material is added at the top in a given time step, then material must be
312 removed at the bottom. This means that the entire section cannot be modeled using one burial

313 condition; if one is interested in the chemical evolution at the top of the section, burial can be
314 turned on. However, if one wants to simulate the evolution at the bottom boundary (i.e., the
315 sediment-basement interface), burial must be zero. In simulations in which burial is applied, a
316 sedimentation rate of ~ 23 m/Ma is utilized, which is the average sedimentation rate for the
317 section over the past ~ 20 Ma (Palike et al., 2010b). In models in which only the last 10.6 Ma is
318 simulated, the burial rate is 23.7 m/Ma.

319 While the model framework permitted solute transport by advection, no advection
320 velocity was applied in the simulations performed given the lack of observational evidence for
321 advection in the sedimentary column. While it is certainly possible that advection occurs in this
322 section, advective fluxes in thick, fine-grained, low permeability carbonate sediments are
323 generally chemically undetectable (Spinelli et al., 2004). Thus we ignore advection; the primary
324 means by which solutes are transported in the fluid is therefore aqueous diffusion. Species-
325 specific diffusion coefficients are defined for all aqueous species at the temperature set for any
326 given simulation (see SI for details). The aqueous ${}^6\text{Li}^+$ and ${}^7\text{Li}^+$ species are assigned nuclide-
327 specific diffusion coefficients that differ, allowing for fractionation during diffusion. The
328 fractionation factor associated with diffusion ($D_{7\text{Li}}/D_{6\text{Li}} = 0.99822$) was determined
329 experimentally (see SI for details) and is similar to previously reported isotopic fractionation
330 factors associated with low-temperature diffusion (i.e., 0.99772 from Richter et al., 2006, and
331 0.991-1.0 from other low temperature studies (Verney-Carron et al., 2011)).

332

333

334

335 4. Results

336 4.1 Lithium Isotopic Compositions ($\delta^7\text{Li}$) of Pore Fluids: Site U1338 Hole A

337 The Li isotopic compositions of pore fluids ($\delta^7\text{Li}$) range between $\sim 28\%$ and $\sim 52\%$ (Fig.
338 3). Delta values are close to that of modern seawater at the top of the section (1.5 rmd) and
339 increase systematically with depth to a maximum value of 51.8% at ~ 325 rmd (Fig. 3). Below
340 this maximum, $\delta^7\text{Li}$ values decrease towards seawater values at the lower sediment-basement
341 interface (Fig. 3). The maximum pore fluid $\delta^7\text{Li}$ value occurs in Unit III, and the most significant
342 rate of change (i.e., $d\delta^7\text{Li}/dz$) occurs close to the boundary between Unit II and Unit III.

343 4.2 Lithium Concentrations and Isotopic Compositions of Sequential Extractions: Site U1338 344 Hole A

345 Sequential extractions of the bulk solid were conducted to understand how Li is
346 apportioned in the bulk sediment. The Li concentration depth profiles of both the exchangeable
347 fraction and the acetic-soluble carbonate are similar to that of the pore fluid (Fig. 4). In order to
348 compare across the various fractions, all concentrations are expressed in mass of Li (ng) per cm^3
349 of porous medium (Table S5 in the supplement contains the mass of Li per g sediment of each
350 sample).

351 Generally, Li concentrations in both the exchangeable and carbonate fractions are in the
352 range of tens to hundreds of ng Li per cm^3 sediment (i.e., comparable to those in the pore fluid;
353 Fig. 4), while Li concentrations in the residual fraction are on the order of thousands of ng
354 Li/ cm^3 sediment (Fig. 4d). Exchangeable Li ranges from ~ 2 to 18 ng Li/ cm^3 sediment through
355 most of the section. The sample closest to the seawater-sediment boundary has a concentration of
356 ~ 200 ng Li/ cm^3 porous medium. Similarly, carbonate concentrations are relatively high at the top

357 (~106 ng Li/cm³) and bottom (~122 ng Li/cm³) of the section and relatively low in between
358 (minimum ~16 ng Li/cm³ sediment between 150 and 250 meters).

359 Lithium concentrations in the HF-soluble residual fraction are significantly higher than
360 either the exchangeable or carbonate fractions; in the upper part of the section (Units I and II),
361 concentrations range between ~350 ng Li/cm³ sediment and ~3,500 ng Li/cm³ sediment at 45
362 rncd. In Unit III, residual Li concentrations generally increase with depth; the maximum
363 concentration is ~4000 ng Li/cm³ sediment at ~381 rncd. The concentration of Li in the sample
364 located near the sediment-basement interface decreases to ~2700 ng Li /cm³ sediment.

365 In these sediments, between 66 and 97% of the total Li is within the silicate phase while
366 the fraction of Li in the carbonate and pore fluid phases ranges between 1 and 10%. The
367 exchangeable fraction typically contains less than 1% of the total Li in each sample except for
368 the sample closest to the seawater-sediment boundary which contains ~15% of the total Li.

369 The Li isotopic compositions of representative extractions were also measured. The
370 exchangeable fraction is enriched in ⁶Li relative to the pore fluids (Fig. 3), ranging from 25 to
371 33‰ with no consistent offset between the pore fluid and exchangeable isotopic compositions.
372 Carbonate isotopic composition is generally similar to seawater, with values ranging between 24
373 and 33‰ and no consistent offset between carbonate and pore fluid. Carbonate $\delta^7\text{Li}$ values
374 increase somewhat with depth, though the trend is noisy. The deepest carbonate, which is located
375 closest to the sediment-basement interface, is isotopically similar to seawater. Residual samples
376 at 1.49, 44.05, and 451.56 rncd have $\delta^7\text{Li}$ values that are significantly lower than corresponding
377 pore fluids (6-11‰), and that increase systematically with depth.

378

379 4.3 Scanning electron microscopy (SEM) and X-ray diffraction (XRD)

380 Scanning electron microscopy (SEM) images of the > 63 μm fraction of the bulk
381 sediment indicate the presence of disk-shaped diatoms surrounded in a biogenic silica
382 (radiolaria/broken diatoms) or carbonate (coccolith) matrix. The carbonate matrix largely
383 consists of coccolithophore plates (see Fig. S2 for additional SEM images of sediment). In most
384 of the sediments imaged, well preserved disk-shaped diatoms are observed (Fig. 5a). Energy
385 dispersive spectroscopy (EDS) analysis (Fig. 5c) indicates that there are insignificant amounts of
386 other cations present in the SiO_2 matrix. In some samples, the disk-shaped diatoms are coated in
387 a material with plate-like structures (Fig. 5b). Analysis via EDS indicates that these particles are
388 aluminosilicates with trace amounts of cations such as Fe and Mg (Fig. 5d).

389 Powder X-ray diffraction (XRD) analysis of several residual extractions was completed
390 in order to identify the presence of clay minerals in the sediment, and supplement IODP smear
391 slide data and core descriptions. Each sample displays multiple peaks at 2θ (5° to 10°) and high
392 d-spacing (16.3 to 16.8; Fig. 5e,f), which is indicative of phyllosilicates (in particular, smectite).

393

394 5 Discussion

395 The data presented in this study support the contention that clay authigenesis occurs in
396 carbonate-rich sediments, and that this process controls the Li geochemistry of the system. In the
397 Discussion that follows, we discuss the evidence for, and present reactive transport models that
398 substantiate, this hypothesis. We then discuss the relevance of clay authigenesis to the global Li
399 cycle, and present reactive transport models that highlight how this process impacts the size and
400 isotopic composition of the authigenic sink over geologic time scales.

401 *5.1 Evidence for chemically-relevant authigenic clay formation at Site U1338*

402 It is clear from the aqueous Li concentration depth profile at Site U1338 that the system
403 is not at a diffusive steady state; such a state would require that the pore fluid Li concentration
404 profile with depth be a straight line connecting the upper and lower boundary conditions. Rather,
405 the Li pore fluid profile is non-linear, indicating that a reactive process must be removing Li in
406 the sedimentary column (and not at the boundaries or by mixing). To confirm that the elemental
407 and isotopic trends are not the result of mixing, pore fluid $\delta^7\text{Li}$ values were plotted against major
408 cation concentrations (Fig. S5). If the isotopic trends were a result of mixing, we would observe
409 binary mixing trends between endmember fluids, such as seawater at the sediment water
410 interface and the basement fluid at the sediment-basement boundary. However, no such trend
411 exists between the deepest and shallowest samples. While trends exist in the pore fluid $\delta^7\text{Li}$ vs
412 pore fluid Si concentration, pore fluid $\delta^7\text{Li}$ vs pore fluid Sr concentration, and pore fluid $\delta^7\text{Li}$ vs
413 pore fluid Li concentration plots, these trends clearly are not related to mixing but reflect the
414 impact of either carbonate recrystallization (Voigt et al., 2015) or clay authigenesis.

415 Several processes could act as the pore fluid Li sink, including surface exchange on clays,
416 carbonate recrystallization, and clay authigenesis. Our sequential extractions suggest that this
417 sink is neither the operationally-defined exchangeable fraction nor the carbonate fraction, as less
418 than 20% of the total Li per sample is contained in the exchangeable or carbonate fraction. While
419 one could argue that such processes occur quickly and therefore the size of the reservoir is
420 unimportant, the mass of Li in these reservoirs is a critical constraint on the potential size of the
421 isotopic effect of a given process on pore fluid $\delta^7\text{Li}$. In addition to the mass constraint, our
422 understanding of the fractionation factors associated with exchange and carbonate
423 recrystallization suggests that neither explain pore fluid $\delta^7\text{Li}$ at Site U1338.

424 Exchange, for instance, occurs quickly relative to the time scale over which the system
 425 evolves, such that a mixing equation is suitable for elucidating its impact on pore fluid $\delta^7\text{Li}$:

$$426 \quad \delta^7\text{Li}_{pf} = \delta^7\text{Li}_{sw} - X_{exchange} \cdot \Delta^7\text{Li}_{exchange-pf} \quad [2]$$

427 where *pf* refers to pore fluid Li reservoir and *exchange* to the surface exchangeable reservoir, Δ^7
 428 $\text{Li}_{exchange-pf}$ is the fractionation factor associated with exchange, X_i is the mole fraction of Li in
 429 the i^{th} reservoir, and we assume that the Li isotopic composition of the system is that of modern
 430 seawater (*sw*). According to Eq. 2, exchange can only have a sizeable effect on pore fluid $\delta^7\text{Li}$ if
 431 the fraction of Li exchanged is large and the fractionation factor is sizeable. At Site U1338,
 432 exchange has neither the mass nor isotopic leverage to explain the pore fluid data.

433 Though carbonate recrystallization requires a different quantitative approach (e.g.,
 434 Richter and DePaolo, 1987), neither the pore fluid nor the carbonate $\delta^7\text{Li}$ values are consistent
 435 with either carbonate recrystallization or net carbonate precipitation as the controlling process,
 436 based on the 6‰ fractionation observed between seawater and core-top carbonates (Pogge von
 437 Strandmann et al., 2019b) and the fractionation factors associated with experimentally-
 438 precipitated carbonate (~3-6‰; Marriott et al., 2004b; Marriott et al., 2004a). The rate of
 439 recrystallization and the elemental partitioning of Li into the diagenetic phase must also be
 440 considered, and we discuss this topic below in more detail.

441 By contrast, the residual HF-soluble fraction, which we assume samples the authigenic
 442 contribution (in addition to any detrital component), has a Li concentration that is two orders of
 443 magnitude larger than the other reservoirs (Fig. 4). Further, the isotopic fractionation associated
 444 with clay formation ($\alpha_{\text{clay-fluid}} \approx 0.972\text{-}0.985$) is sizeable and, combined with the assumption of
 445 the mass flux associated with clay authigenesis, can explain the pore fluid $\delta^7\text{Li}$ data.

446 A range of supplemental evidence supports the contention that Li is removed by clay
447 authigenesis at Site U1338. Clay formation preferentially incorporates ^6Li (Pistiner and
448 Henderson, 2003; Vigier et al., 2008; Wimpenny et al., 2015), increasing pore fluid $\delta^7\text{Li}$ values
449 in fluids that are not in diffusive communication with either the upper or lower boundaries. At
450 Site U1338, pore fluid $\delta^7\text{Li}$ values are considerably higher at depth relative to seawater; the
451 highest delta value is $\sim 52\text{‰}$ at 325 mcd (or $\sim 20\text{‰}$ higher than seawater). Additional evidence
452 for clay formation is the low $\delta^7\text{Li}$ value of the residual phase (Fig. 3). As we will discuss in more
453 detail below, an increase in pore fluid $\delta^7\text{Li}$ with depth in the sedimentary section is expected due
454 to clay authigenesis.

455 In addition, while smear slide observations suggest that the residual fraction consists of
456 diatoms and radiolaria (Palike et al., 2010b), the measured Li concentrations in the HF residual
457 fraction cannot be explained by biogenic silica, which is assumed to have Li concentrations less
458 than 2 ppm (Chan and Kastner, 2000). All of the residual samples have concentrations greater
459 than 2 ppm, strongly suggesting the presence of an HF-soluble siliciclastic phase in addition to
460 biogenic silica and detrital clay. Authigenic clays can have Li concentrations of 50-100 ppm with
461 a maximum concentration of ~ 500 ppm Li (Hein et al., 1979; Chan et al., 2006; Vigier et al.,
462 2008), nearly an order of magnitude larger than the Li concentration in detrital clays (Zhang et
463 al., 1998).

464 We estimate the relative contribution of each component by mass balance using the mass
465 of Li in the residual fraction measured at Site U1338 and assuming Li concentrations in the
466 biogenic silica (2 ppm) and authigenic (500 ppm) or continentally-derived/detrital (50 ppm) clay
467 endmembers (Table 1). Given these assumptions, the maximum proportion of authigenic clay
468 ranges from ~ 1 -5% throughout the section. If continentally-derived clay is the only component

469 that is mixed with biogenic silica, then the maximum proportion of detrital clay is 40%. We
470 conclude that this value is too high to have been missed in smear slide observations, and thus
471 suggest that this supports the contention that the Li geochemistry reflects the presence of
472 authigenic clay at Site U1338. Though detrital clays may be present in the section, we contend
473 that they do not explain the Li geochemical trends that we observe.

474 Altogether, the data presented above support the contention that biogenic silica (mainly
475 diatoms) facilitates the precipitation of authigenic clay minerals at Site U1338. Such a hypothesis
476 is consistent with studies of coastal sediments near the Amazon River outflow, which inferred a
477 similar process to be occurring (Michalopoulos et al., 2000; Michalopoulos and Aller, 2004).
478 Our observations, however, indicate that this process is not restricted to shallow deltaic
479 sediments but could also be important in deep-sea carbonate sediments. Such a hypothesis has a
480 range of implications for proxy archives and the global Li cycle, which we discuss in detail
481 below.

482 A reactive transport modeling approach was utilized to evaluate whether or not
483 authigenic clay formation is appropriate for explaining the observed Li and $\text{SiO}_2(\text{aq})$
484 concentration and Li isotopic profiles. The model takes into account gross differences in porosity
485 and amorphous silica ($\text{SiO}_2(\text{am})$) concentration with depth in the column (i.e., between Units I/II
486 and Unit III). In all simulations shown (Fig. 6), the fractionation factor associated with diffusion
487 is 0.9982, burial is assumed to be constant ($=23.7 \text{ m Ma}^{-1}$), and the initial pore fluid Li
488 concentration and $\delta^7\text{Li}$ is 26 μm and 31.5‰, respectively. The authigenic solid is assumed to be
489 unreactive after precipitation, and the lower boundary is open to diffusion. The model is run for
490 10.6 Ma, and is initially comprised of a 450-meter section that has similar porosity (0.634) and
491 biogenic silica content (10.8 wt. %; 2 ppm Li) as Unit III (89.2 wt. % Li-free carbonate). The

492 simulation then buries the initial sediments with sediment that has a porosity of 0.767, a biogenic
493 silica content of 23.8 wt. %, and a carbonate content of 79.2 wt. % (i.e., similar to Units I and II).
494 During the simulation, biogenic silica dissolves and reprecipitates as an authigenic clay mineral
495 that has a Li concentration of 500 ppm, with variable $\alpha_{\text{clay-fluid}}$ (in these simulations, we create a
496 “basecase” simulation for comparison where $\alpha_{\text{clay-fluid}}$ is 0.986; Pistiner and Henderson, 2003).
497 As there is no constraint on the identity of the authigenic phase forming at Site U1338, and no
498 pore fluid Al data are available, we have chosen an authigenic clay phase (hectorite) that consists
499 of Si, Na, Mg, and Li ($4\text{H}_2\text{O} + 4\text{SiO}_2(\text{aq}) + 0.03\text{Li}^+ + 0.03\text{Na}^+ + 2.97 \text{Mg}^{++} \rightarrow$
500 $(\text{Mg,Li,Na})_3\text{Si}_4\text{O}_{10}(\text{OH})_2 + 6\text{H}^+$). Saturation state calculations indicate that the pore fluid is
501 supersaturated with respect to this mineral at all depths.

502 Generally, the model reproduces the major features of the Li concentration and isotopic
503 profiles. However, the Li isotopic composition of the pore fluid in Unit III is poorly fit when we
504 assume a fractionation factor of ~ 0.986 , an average of fractionation factors associated with
505 secondary mineral precipitation and, more generally, basalt interaction with seawater (0.972 to
506 0.999; Chan et al., 1992; Pogge von Strandmann et al., 2008; Wimpenny et al., 2015) and
507 comparable to that associated with smectite precipitation at low temperatures (0.990 ± 0.0013 ;
508 Vigier et al., 2008), and equal reactivity of authigenic clay in the upper and lower units (Fig. 6a).
509 In this case, the term 'reactivity' refers to the fundamental controls on authigenic precipitation
510 rate aside from saturation state (i.e., surface area and intrinsic rate constant). In light of this
511 discrepancy, there are two likely means by which the pore fluid $\delta^7\text{Li}$ trend with depth at Site
512 U1338 can be explained: (i) an increase in authigenic clay reactivity in Unit III or (ii) a
513 fractionation factor that varies with depth. The observed discrepancy can also be explained by a
514 different Li stoichiometry in the authigenic clay in Units I/II and Unit III, though this is an effect

515 that we do not attempt to simulate given the lack of constraints on the composition of the
516 authigenic phase.

517 An increase in authigenic clay reactivity by $\sim 20x$ in Unit III relative to Units I/II is
518 sufficient to explain the Li isotopic composition of the pore fluids (Fig. 6b). In the model, the
519 reactivity increase is generated by an increase in the specific surface area of the precipitating
520 clay in Unit III, though the overall precipitation rate is a function of both the saturation state and
521 rate constant as well as specific surface area. In the enhanced reactivity scenario (Fig. 6b), the
522 model precipitation rates were generally higher by no more than a factor of 2 in Unit III
523 compared to Units I/II, though this difference varied as a function of the saturation state with
524 depth. Our observation is that enhanced reactivity is consistent with the Li concentration profile
525 and, while the pore fluid Li concentration profile is slightly less well fit in Units I/II, the
526 asymmetry of the depth trend is captured.

527 A different fractionation factor between Units I/II and Unit III can also explain the pore
528 fluid $\delta^7\text{Li}$ trend with depth. If the fractionation factor is ~ 0.995 in Units I/II and ~ 0.980 in Unit
529 III, the general shape of the depth trend can be approximated (Fig. 6d). Such values are generally
530 consistent with Li isotopic fractionation associated with secondary mineral formation, but are
531 significantly different from experimental constraints on fractionation associated with smectite
532 precipitation (Hindshaw et al., 2019). We stress that our constraint on the fractionation factor is
533 general; we do not know the mineralogy of the precipitating phases nor have we simulated
534 carbonate recrystallization and clay authigenesis together.

535 Nonetheless, the critical observation we make in comparing the two hypotheses is that it
536 is difficult to match the sharpness of the $\delta^7\text{Li}$ profile by varying the fractionation factor, unlike in
537 the case of faster clay precipitation rates in Unit III. This is because the balance between

538 diffusion and reaction, which is constrained by the Li concentration trend with depth, is the same
539 in Units I/II and Unit III in the case of variable fractionation factor, unlike the variable reactivity
540 scenario. As the rates of clay precipitation and biogenic silica dissolution increase, the diffusive
541 reaction length scale decreases and allows for the maintenance of steeper concentration and
542 isotopic gradients. Thus, we contend that the features of the $\delta^7\text{Li}$ pore fluid profile support the
543 hypothesis that authigenic clay precipitation rates are significantly higher in Unit III relative to
544 Units I/II.

545 Overall, the modeling suggests that authigenic clay formation can explain the Li
546 elemental and isotopic geochemistry at Site U1338. Our simulations are consistent with ~1 vol.
547 % authigenic clay in Site U1338 carbonate sediments, but this value will vary if the
548 stoichiometry of the authigenic phase that we assume to be forming changes. In addition, it is
549 notable that reactivity changes in the sedimentary column complicate efforts to constrain
550 mineral-aqueous fractionation factors from pore fluid data. Using Site 1338 as an example, one
551 could interpret the change in pore fluid $\delta^7\text{Li}$ as reflecting a change in fractionation factor (and
552 thus process and/or mineralogy), when it could simply reflect a change in mineral reactivity at
553 depth (which does not require a change in process). The interpretations in these two cases are
554 thus entirely distinct.

555

556 *5.2 Implications of authigenic clay formation in carbonate-rich sections for the global Li cycle*

557 If marine authigenic clay formation is important globally, then this process can, in some
558 cases, generate a significant flux that removes Li from the ocean. This is due to the fact that
559 authigenic clay minerals can incorporate hundreds of micrograms of Li per gram of clay (Hein et

560 al., 1979), compared to the tens of $\mu\text{g Li/g}$ clay typical in detrital clays (Zhang et al., 1998). Clay
561 authigenesis, therefore, has the potential to impact the global Li cycle (Chan et al., 1992; Chan et
562 al., 2002; Hathorne and James, 2006). In order to estimate the size of such a flux, we explore Li
563 pore fluid concentration gradients throughout the modern ocean and attempt to outline the major
564 controls on those gradients. Our objectives are to predict how such a flux might change over
565 geologic time scales and to discuss what may drive such changes.

566

567 *5.2.1 Controls on the Li concentration gradient in marine pore fluids*

568 The global Li cycle is often considered to be at steady state (Stoffyn-Egli and Mackenzie,
569 1984; Huh et al., 1998; Hathorne and James, 2006; Misra and Froelich, 2012), and the reverse
570 weathering flux calculated as a consequence of this assumption. Of the major inputs of Li to the
571 modern ocean, the riverine flux has been estimated to be between $8 \cdot 10^9$ moles Li/a (Huh et al.,
572 1998) and $1 \cdot 10^{10}$ moles Li/a ($\delta^7\text{Li} \sim 23\%$) (Misra and Froelich, 2012). The hydrothermal flux
573 has been estimated to be between $6 \cdot 10^9$ moles Li/a (Hathorne and James, 2006) and $1.3 \cdot 10^{10}$
574 moles Li/a ($\delta^7\text{Li} \sim 8.3\%$) (Misra and Froelich, 2012), and the subduction reflux has been
575 estimated to be $\sim 0.6 \cdot 10^{10}$ moles Li/a ($\delta^7\text{Li} \sim 15\%$) (Misra and Froelich, 2012). The total input
576 flux thus ranges between $\sim 1.4 \cdot 10^{10}$ and $2.9 \cdot 10^{10}$ moles Li/a (Hathorne and James, 2006; Misra
577 and Froelich, 2012).

578 Lithium is removed from the modern ocean via the formation of secondary silicate
579 minerals in the sedimentary column or during the alteration of basalts. To maintain steady state,
580 these output fluxes must be on the order of 10^{10} mol Li/a. Little appears to be known about how
581 the output flux is apportioned in the modern ocean, and what controls the distribution between

582 the two main sinks; it has been suggested that the two sinks in the modern ocean are
583 approximately equivalent and that shifts between them can account for at least some of the
584 variability in the evolution of seawater $\delta^7\text{Li}$ over the Cenozoic (Li and West, 2014). Insight into
585 the controls on these sinks is critical, as it allows us to infer how such fluxes may vary over
586 geologic time scales and, therefore, to evaluate how reasonable hypotheses invoking authigenic
587 shifts may be. Because these inferences are crucial to interpreting the Li isotope proxy, we
588 explore the marine authigenic sink in some detail.

589 In the modern ocean, Li concentration profiles in marine sections generally either
590 decrease with depth or increase with depth (Fig. 7b-d), a feature that is generally dictated by the
591 balance between detrital silicate dissolution and authigenic clay precipitation. Profiles that
592 decrease with depth are observed in carbonate-rich sediments and volcanogenic sediments (Fig.
593 7b; e.g., Zhang et al., 1998; You et al., 2003). Profiles that increase with depth are often found in
594 terrigenous and convergent margin sediments, in which the Li dissolution flux exceeds the
595 precipitation flux (Fig. 7c; e.g., Martin et al., 1991; You et al., 1995; Zhang et al., 1998; Chan
596 and Kastner, 2000). To begin to understand the distribution of these profiles and their impact on
597 the global Li cycle, a survey of Li concentration profiles and lithology (mainly % CaCO_3) was
598 conducted. Our general finding is that pore fluid Li concentration trends with depth are steepest
599 at sites with high CaCO_3 contents (decreasing with depth), while there is considerably more
600 variability at sites where siliciclastic contents are higher. This observation is consistent with the
601 control of Li pore fluid concentration gradients by lithology.

602 A compilation of all ODP and IODP sites with Li concentration data extending more than
603 50 meters below seafloor suggests that Li sinks are distributed globally throughout the ocean.
604 (Fig. 7a). Of the 267 sites that were categorized, 78 sites are sinks, 60 sites are sources of Li to

605 the ocean, and 129 are hybrids that have low to sink-like slopes in the upper 50-100 meters but
606 increase in concentration at depth. It is unclear if the hybrid sites are at steady state, a topic we
607 address below. Broadly speaking, sink sites are located in the open ocean, while both source and
608 hybrid sites are typically located close to land/continental margins (Fig. 7a). The geographical
609 distribution generally supports the hypothesis that sink sites are a consequence of dominant
610 secondary mineral precipitation relative to silicate dissolution; ostensibly, this is a consequence
611 of low terrigenous input relative to biogenic silica input in the open ocean. The sites that act as
612 sinks near continental margins and in siliciclastic sediments have previously been discussed
613 (e.g., Stoffyn-Egli and Mackenzie, 1984 and Zhang et al., 1998) and will not be discussed
614 further here.

615 Ultimately, we hypothesize that carbonate-rich sediments exhibit Li concentration
616 profiles that decrease with depth because the flux of Li into precipitating authigenic clays is
617 greater than the flux from dissolving carbonate, detrital clays and/or biogenic silica.
618 Accordingly, Li concentration gradients in carbonate-rich sediments have the potential to be
619 steep, and carbonate-rich sediments could therefore be significant Li sinks from the ocean within
620 the global Li cycle.

621

622 *5.2.2 Quantifying the Li sink in carbonate-rich sediments and assessing its secular variability*

623 To elucidate the importance of this diffusive flux within the global Li cycle, and to assess
624 those factors that may drive secular variability in this output flux, we utilized simple calculations
625 and reactive transport simulations to estimate the size and isotopic composition of the global
626 output flux of Li as well as the secular evolution of the flux. Diffusive mass fluxes (F , in units of

627 moles per unit area per time) calculated from pore fluid Li concentration profiles using Fick's
628 First Law ($F = -\phi \cdot D \cdot dC/dz$, where $D = 6.84 \cdot 10^{-6} \text{ cm}^2/\text{s}$; e.g., Berner, 1980) ranged from $1.4 \cdot 10^{-6}$
629 to $4.5 \cdot 10^{-4} \text{ mol Li/m}^2/\text{a}$, depending on the length scale over which the Li concentration gradient
630 was imposed (1 to 250 m) and the porosity (0.6 to 0.8), If we consider seawater Li concentrations
631 as much as five times the modern value, then the flux estimates increase to $\sim 6.7 \cdot 10^{-6}$ to $2.2 \cdot 10^{-3}$
632 $\text{mol Li/m}^2/\text{a}$.

633 If we assume that this mechanism operates in carbonate sediments over the entire surface
634 area of the ocean (excluding continental shelves: $\sim 3.1 \cdot 10^8 \text{ km}^2$), the *maximum* removal flux in
635 carbonate sediments is $\sim 1.4 \cdot 10^{11} \text{ moles Li/a}$ assuming a porosity of 0.8 and a seawater Li
636 concentration of $26 \text{ }\mu\text{M}$ ($F = 7 \cdot 10^{11} \text{ mol Li/a}$ if we assume 5x modern Li seawater concentration).
637 If we assume a porosity of 0.7 and the maximum concentration gradient (i.e., from $26 \text{ }\mu\text{M}$ to 0)
638 over 10-100 meters, then the flux estimate is $\sim 1.2 \cdot 10^9$ to $1.2 \cdot 10^{10} \text{ mol Li/a}$, which is comparable
639 to the total removal flux cited by Hathorne and James (2006) and Misra and Froelich (2012).
640 With regard to the modern ocean ($26 \text{ }\mu\text{M}$, $1.46 \cdot 10^{21} \text{ kg}$, $3.8 \cdot 10^{16} \text{ mol Li}$), this equates to a ~ 3 -30
641 Ma time scale ($\tau = N/F$, where N is the moles of Li in the ocean and F is the flux in mol/Ma)
642 over which this flux impacts the isotopic evolution of the ocean.

643 More interestingly, the output mass flux and isotopic composition of this flux may vary
644 over time, a feature that we illustrate using reactive transport simulations. In particular, the
645 secular variability in the isotopic composition of the authigenic output flux is controlled by the
646 depth in the sedimentary column at which, and the extent to which, Li precipitates in clays. In the
647 model simulations, this is illustrated by two scenarios in which reactive $\text{SiO}_2(\text{am})$ is buried and
648 dissolves in the sedimentary column, generating a chemical drive to precipitate authigenic clay
649 (Fig. 8). In the first scenario, reactive $\text{SiO}_2(\text{am})$ is buried continuously from 2.5 Ma to 20 Ma; in

650 the second scenario, the reactive zone is discrete and moves through the column as burial occurs
651 at the upper boundary. The two scenarios yield considerable differences in pore fluid
652 geochemistry, some of which are due to the fact that the rate constants are the same for the
653 reactive zones in both cases but the size of the reactive zones is different between the two cases,
654 resulting in a considerable difference in the amount of integrated reaction in the two scenarios.

655 Regardless, the models clearly support the contention that isotopic distillation, due to
656 isotopic fractionation associated with clay precipitation, occurs in the pore fluid at depth if the
657 solid does not back-react (or back-reacts slowly) with the pore fluid. Distillation is most
658 pronounced far from boundaries, such as the seawater-sediment and sediment-basement
659 interfaces, where diffusive input of Li to the pore fluid is unable to keep pace with Li removal by
660 clay precipitation (e.g., Fantle et al., 2020). The effect of distillation at depth in the sedimentary
661 column is to generate an output flux that is isotopically closer to seawater than would be
662 assumed on the basis of experimental fractionation factors. For instance, the isotopic
663 fractionation associated with the “reverse weathering” output flux has been cited as ranging
664 between -14 and -16‰, based (at least in part) on isotopic fractionation factors constrained by
665 laboratory experiments (e.g., Pistiner and Henderson, 2003; Vigier et al., 2008; Hindshaw et al.,
666 2019). Our simulations suggest that this constraint may not accurately reflect the bulk of the
667 authigenic output flux, and that isotopic distillation at depth modifies the effective fractionation
668 factor of the output flux. Such fractionation factors would explain authigenesis occurring near
669 the seawater-sediment interface, but that is likely negligible.

670 The simulations suggest a predictable and systematic means by which the isotopic
671 composition and size of the authigenic output flux may vary over time. In the continuous burial
672 scenario (Fig. 8a-d; Fig. 9a), the mass output flux increases in time as more reactive biogenic

673 silica is buried. As a consequence, the pore fluid Li concentration gradient steepens and the
674 diffusive mass flux of Li out of the ocean increases. At the same time, the extent of isotopic
675 distillation increases, as the integrated depth over which authigenesis occurs also increases.
676 Thus, the isotopic composition of the output flux becomes less fractionated relative to seawater,
677 reducing the leverage of authigenesis to change seawater $\delta^7\text{Li}$. In the discrete burial scenario
678 (Fig. 8e-h; Fig. 9b), the zone of authigenesis moves steadily away from the sediment-seawater
679 interface, increasing the length scale of communication with the overlying water column. At a
680 given mass flux, this generates considerably more distillation than in the continuous burial case,
681 which has reactive solid over a range of depths (some of which are close to seawater-sediment
682 boundary and some of which are farther).

683 Ultimately, we have shown that the Li isotopic composition of the output flux associated
684 with clay authigenesis is not simply related to experimental fractionation factors, but is altered
685 by isotopic distillation in the sedimentary column. Consequently, the $\delta^7\text{Li}$ value of this flux can
686 vary in time as a function of the depth in the sedimentary column where authigenesis occurs and
687 the relative mass of Li removed from the pore fluid. Given the significant size of the mass flux,
688 this mechanism should be considered when interpreting secular trends of seawater $\delta^7\text{Li}$.

689

690 *5.3 Implications of clay authigenesis for the use of Li isotopes as a geochemical proxy*

691 The current study has implications for the interpretation of the Li isotope proxy in
692 carbonate archives. Carbonate recrystallization in the presence of pore fluid with non-seawater
693 $\delta^7\text{Li}$ values can shift the $\delta^7\text{Li}$ of the carbonate (Fantle and DePaolo, 2007; Fantle and Higgins,
694 2014; Fantle, 2015):

$$d\delta_{solid} = -R[(\delta_{solid} - \delta_{fluid}) - \Delta_{s-f}^{diag}]dt \quad [3]$$

696 where $d\delta_{solid}$ is the change in the isotopic composition of carbonate mineral as a consequence of
 697 recrystallization (at a given rate, R) at isotopic disequilibrium ($(\delta_{solid} - \delta_{fluid}) - \Delta_{s-f}^{diag} \neq 0$) over
 698 time (dt). The term Δ_{s-f}^{diag} is the fractionation factor between carbonate solid (s) and the aqueous
 699 species in the fluid (f) under diagenetic conditions, which may differ from that associated with
 700 formation.

701 Diagenetic recrystallization can impact the Ca and Mg isotopic composition of
 702 carbonates (Fantle and Higgins, 2014; Chanda and Fantle, 2017), as well as the $^{87}\text{Sr}/^{86}\text{Sr}$ ratio
 703 (Fantle, 2015; Chanda and Fantle, 2017). Lithium may be particularly susceptible to alteration,
 704 as its diffusive reaction length ($\sqrt{D/RMK}$, where D is the diffusion coefficient, R is the
 705 recrystallization rate, M is the solid/fluid mass ratio, and K is the elemental partition coefficient)
 706 is relatively long (~ 600 m) compared to other carbonate-relevant elements such as Ca (~ 15 m)
 707 and Sr (~ 150 m) (Fantle and DePaolo, 2006; Fantle et al., 2020). Despite the importance of
 708 understanding the impact of recrystallization on the Li isotopic composition of carbonate
 709 archives that are the basis for paleoclimatic and paleoenvironmental reconstructions, there are
 710 few studies of this type (Ullmann et al., 2013; Dellinger et al., 2020).

711 We investigate the hypothesis that recrystallization can explain bulk carbonate $\delta^7\text{Li}$ at
 712 Site U1338 using a depositional carbonate recrystallization model that has been described
 713 previously (e.g., Fantle and DePaolo, 2006). In our simulations, we assume initial Li
 714 concentrations of deposited carbonate ($< 30 \mu\text{mol/kg}$ solid) and recrystallization rates constrained
 715 by our modeling of Sr and Sr isotopes
 716 (*Fig. S3*; rate [g reacted g solid $^{-1}$ Ma^{-1}] = $0.07 \cdot e^{-age/5.25}$) that are consistent with those of

717 Voigt et al. (2015). The model simulations suggest that it is not possible to explain the bulk
 718 carbonate Li geochemistry as a consequence of recrystallization alone (Fig. 10). In addition, at
 719 these recrystallization rates, and assuming a diagenetic fractionation factor of ~ 0.9955 (Marriott
 720 et al., 2004b; Marriott et al., 2004a), neither the pore fluid Li concentrations (Fig. 10a) nor $\delta^7\text{Li}$
 721 values (Fig. 10b) can be explained, even considering a large range in the partition coefficient
 722 ($K_{d,\text{Li}} = (m_{\text{Li}}/m_{\text{Ca}})_{\text{solid}} / (m_{\text{Li}}/m_{\text{Ca}})_{\text{aq}} = 3 \cdot 10^{-3}$ to $3 \cdot 10^{-2}$). Carbonate recrystallization alone is also
 723 not sufficient to explain the bulk carbonate (i) Li concentration (Fig. 10c-d) or (ii) Li isotopic
 724 composition trends with depth (Fig. 10e-f).

725 Though we cannot say with certainty what the Li concentration of primary bulk carbonate
 726 is in the section, a simple mass balance analysis suggests that the Li concentration of primary
 727 bulk carbonate is not a uniform $\sim 40 \mu\text{mol/kg}$ with depth (i.e., similar to sediments at the top of
 728 the section):

$$729 \quad \left(\frac{N^{\text{Li}}}{N^{\text{Ca}}} \right)_{\text{meas carb}} = X_{\text{primary}}^{\text{Ca}} \left(\frac{N^{\text{Li}}}{N^{\text{Ca}}} \right)_{\text{primary}} + X_{\text{recrystallized}}^{\text{Ca}} \left(\frac{N^{\text{Li}}}{N^{\text{Ca}}} \right)_{\text{recrystallized}} \quad [4]$$

730 where, N^i/N^j is the molar ratio of element i to element j . If we assume a primary Li/Ca of ~ 4
 731 $\mu\text{mol/mol}$ in bulk carbonates, then we must explain measured Li/Ca as low as 1. Yet, assuming a
 732 theoretical minimum $K_{d,\text{Li}}$ of 0, mass balance limits the recrystallized bulk carbonate to a
 733 minimum Li/Ca of 2.4. Values lower than 2.4 must be explained by alternate means. Therefore,
 734 we contend that the initial Li/Ca of the nannofossil ooze at Site U1338 is actually ~ 0.1 (< 10
 735 $\mu\text{mol/kg}$ solid), which is considerably lower than other biogenic carbonates (Dellinger et al.,
 736 2018).

737 Consequently, we can qualitatively explain bulk carbonate $\delta^7\text{Li}$ at Site U1338 if we
738 assume that initial bulk carbonate Li concentrations are generally relatively low, and that
739 carbonate recrystallization operates in the presence of clay authigenesis. Clay authigenesis
740 controls pore fluid $\delta^7\text{Li}$, and establishes the isotopic leverage to alter carbonate during
741 recrystallization at depth in the sedimentary column. Near the seawater-sediment interface,
742 however, the decrease in $\delta^7\text{Li}$ relative to the global seawater curve reflects isotopic equilibration
743 of the solid with pore fluid with a seawater-like $\delta^7\text{Li}$ ($\alpha_{\text{carbonate} - \text{fluid}} = 0.9955$). The increase
744 lower in the section then reflects re-equilibration with a fractionated pore fluid ($\delta^7\text{Li} \sim 55\text{‰}$).
745 Further, because explaining relatively high bulk carbonate Li concentrations in the uppermost
746 part of the section is difficult without invoking some temporal variability in the bulk solid (which
747 we deem unlikely over the inferred time scales), we hypothesize that a greater proportion of
748 foraminiferal tests with higher Li concentrations in the upper ~ 100 meters of the section accounts
749 for the higher Li concentrations in the upper ~ 75 meters of the section.

750 There are two possibilities regarding the location of the high pore fluid $\delta^7\text{Li}$ in the
751 sedimentary section, which we designate the 'reactive zone' (Fig. 10k): (1) that it always occurs
752 at depth in the section, or (2) that it moves from the seawater-sediment interface to depth over
753 time. If we assume that the reactive zone is always relatively deep in the column, then
754 recrystallization does not explain the observations at the detailed level, and the modeled solid
755 looks similar to the recrystallization-only scenarios (Fig. 10a-f). Specifically, the diagenetic shift
756 in $\delta^7\text{Li}$ is negligible (Fig. S4) because the carbonate does not recrystallize significantly in the
757 lower part of the section.

758 Thus, there are two ways to explain our observations: (1) the reactive zone has shifted its
759 location over time or (2) the pore fluid over the past ~17.5 Ma has been significantly more
760 distilled than it is today. We explore the first hypothesis, as the second is limited by the
761 likelihood that pore fluid Li concentrations are $>1 \mu\text{M}$ (which limits the distillation effect; note
762 that the distillation effect is impacted by changes in the reaction rate relative to the diffusive flux
763 and/or the initial pore fluid Li concentration). In the model, we do not model clay authigenesis
764 explicitly, but crudely approximate its effect on both pore fluid Li concentrations and $\delta^7\text{Li}$ by
765 assigning a reactive zone in which Li concentrations and isotopic compositions can be
766 maintained at values that are constant or vary over time (Fig. 10i-j). Because of the limited
767 functionality with regard to simulating clay authigenesis, the resulting simulations are meant
768 only to ascertain if recrystallization in the presence of clay authigenesis can explain the observed
769 carbonate $\delta^7\text{Li}$ trend and what that would require.

770 Based on our modeling efforts (Fig. 10g-h), we can explain the $\delta^7\text{Li}$ of the carbonate
771 fraction at Site U1338 by assuming that the reactive zone has migrated from the seawater-
772 sediment interface to its current depth over the past ~10-11 Ma. This is consistent with the
773 concept that clay authigenesis is promoted by biogenic silica, and that this process is not
774 necessarily constant in time. Interestingly, carbonate $\delta^7\text{Li}$ records the movement of the reactive
775 zone, which suggests bulk nannofossil ooze $\delta^7\text{Li}$ as a recorder of clay authigenesis in the
776 sedimentary column.

777 It is also possible that the Li isotopic composition of carbonates is impacted by
778 siliciclastic contamination, which is especially problematic in cases in which the mass balance
779 favors the contaminating phase. We suggest that that the study of You et al. (2003), who
780 analyzed bulk carbonate and pore fluids at Site 851, is an example of the impact of clay

781 contamination on bulk nannofossil ooze $\delta^7\text{Li}$. While Sites 851 and U1338 have similar
782 lithologies and pore fluid Li concentration and $\delta^7\text{Li}$ depth profiles, bulk carbonate $\delta^7\text{Li}$ values at
783 Site U1338 are quite different from those at Site 851 (Fig. 11a).

784 Various lines of evidence support our interpretation that bulk carbonate measurements at
785 Site 851 are impacted by clay contamination. First, bulk carbonates at Site U1338 are
786 isotopically similar to modern seawater, which is the expectation for marine carbonates (Hall et
787 al., 2005; Vigier et al., 2007). By contrast, the bulk carbonates from Site 851 have exceedingly
788 low $\delta^7\text{Li}$ values, in the range of the residual silicates at Site U1338 (Fig. 3). Second, the
789 interpretation put forth by You et al. (2003) was that the bulk carbonate $\delta^7\text{Li}$ depth profile was a
790 result of carbonate recrystallization. In this case, recrystallization would have to be close to
791 100% at ~250 meters, which is an extent of recrystallization not seen in modern nannofossil
792 oozes (Fantle and DePaolo, 2006; Fantle and DePaolo, 2007; Fantle et al., 2010; Fantle, 2015).
793 And finally, recent work has demonstrated that small quantities of clay have sufficient leverage
794 to alter the $\delta^7\text{Li}$ of bulk carbonates (Pogge von Strandmann et al., 2013).

795 Our data suggest that our measurements of $\delta^7\text{Li}$ are not impacted by clay contamination,
796 as the measured carbonate Li concentrations are quite low. Further, comparisons of our
797 carbonate $\delta^7\text{Li}$ to previously measured foraminiferal $\delta^7\text{Li}$, especially in Unit III, support the
798 interpretation that bulk carbonate $\delta^7\text{Li}$ at Site U1338 reflects the impact of a post-depositional
799 process (Fig. 11b; Hathorne and James, 2006; Misra and Froelich, 2012). Thus, we conclude that
800 carbonate recrystallization in the presence of clay authigenesis explains the bulk carbonate data
801 at Site U1338.

802

803 **6 Conclusions**

804 The Li isotopic composition ($\delta^7\text{Li}$) of pore fluids sampled from a carbonate-rich site
805 (IODP Site U1338) are presented and interpreted to reflect clay authigenesis in the sedimentary
806 column. Clay authigenesis sequesters Li in secondary clays, lowering pore fluid Li
807 concentrations and generating Li concentration profiles that decrease strongly with depth and
808 $\delta^7\text{Li}$ values that increase strongly with depth. Reactive transport models suggest that clay
809 authigenesis, and not carbonate recrystallization, controls pore fluid $\delta^7\text{Li}$; at a finer scale, the
810 $\delta^7\text{Li}$ depth profile is best explained by an increase in reactivity (i.e., clay precipitation rate) at
811 depth, and not changes in the isotopic fractionation factor associated with clay precipitation.
812 Elucidating the control on the Li isotopic composition of marine pore fluids is important, as this
813 signal can impact the $\delta^7\text{Li}$ of both siliciclastic proxy archives and carbonate proxy archives (i.e.,
814 via authigenesis, recrystallization, and/or contamination by siliciclastics).

815 We interpret the $\delta^7\text{Li}$ of chemically-cleaned carbonate at Site U1338 to be a consequence
816 of recrystallization, but only in the presence of an active zone of clay authigenesis in the
817 sedimentary column; recrystallization alone cannot explain carbonate $\delta^7\text{Li}$, which is consistent
818 with our interpretation of pore fluid $\delta^7\text{Li}$. Using numerical models of carbonate recrystallization,
819 we hypothesize that the reactive zone of clay authigenesis has moved from the surface to its
820 current location over the past 10-11 Ma. This model-constrained conclusion provides support for
821 the hypothesis that the isotopic composition of the authigenic clay sink for Li has varied over
822 time.

823 The observations above are important because they highlight the role that clay
824 authigenesis, particularly in carbonate-rich sections, could play in the global Li cycle. Assuming

825 that clay authigenesis occurs to some extent in all carbonate-rich sections, we estimate that the
826 output flux of Li into carbonate-rich sediments could reasonably be as large as $\sim 1.2 \cdot 10^{10}$ moles
827 Li per year, which is similar to previous estimates of the mass flux required to balance the
828 modern Li budget. In theory, then, clay authigenesis in carbonate-rich sections may be a
829 significant contributor to the global Li cycle.

830 Moreover, it is often assumed that the Li isotopic composition of the authigenic sink is
831 simply related to the isotopic composition of seawater, modified by a fractionation factor (e.g.,
832 Misra and Froelich, 2012). However, this is only true when the reaction occurs at the seawater-
833 sediment interface. When the reaction occurs at depth, the pore fluid undergoes isotopic
834 distillation, which has two significant effects: (1) it reduces the leverage of clay authigenesis to
835 change seawater $\delta^7\text{Li}$, and (2) the movement of the reactive zone relative to the seawater-
836 sediment interface drives secular variability in the $\delta^7\text{Li}$ of the output flux. Consequently, this
837 process, which is impacted by the reactivity of biogenic silica (or, in coastal sections,
838 continentally-derived silicate) and the relative rates of burial, transport, and reaction, can drive
839 long-term (i.e., on time scales of ~ 3 -30 Ma, depending on the mass flux that one assumes)
840 changes in the $\delta^7\text{Li}$ of seawater. Ultimately, then, this flux must also be considered in
841 interpretations of proxy records, including the seawater $\delta^7\text{Li}$ record over the Cenozoic.

842

843 **7 Acknowledgements**

844 We would like to thank Ed Hathorne for providing squeeze-cake samples, and Jared Carte and
845 Matthew Gonzales for laboratory assistance. This manuscript was greatly improved by the

846 comments of two anonymous reviewers and AE James. Funding for this work was provided by
847 the National Science Foundation grant number 1446271 to MSF. PPvS and analyses at LOGIC
848 were funded by ERC Consolidator grant 682760 CONTROLPASTCO2.

Journal Pre-proofs

849 **References**

- 850 Apitz S. E. (1991) The Lithification of Ridge Flank Basal Carbonates: Characterization and Implications for
851 Sr/Ca and Mg/Ca in Marine Chalks and Limestones. University of California, San Diego.
- 852 Berner R. (1980) *Early Diagenesis A Theoretical Approach.*, Princeton University Press, Princeton.
- 853 Burton K. W. and Vigier N. (2012) Lithium Isotopes as Tracers in Marine and Terrestrial Environments. In
854 *Handbook of Environmental Isotope Geochemistry: Vol I* (ed. M. Baskaran). Springer Berlin
855 Heidelberg, Berlin, Heidelberg. pp. 41–59.
- 856 Chan L.-H., Leeman W. P. and Plank T. (2006) Lithium isotopic composition of marine sediments.
857 *Geochemistry, Geophys. Geosystems* **7**.
- 858 Chan L. H., Alt J. C. and Teagle D. A. H. (2002) Lithium and lithium isotope profiles through the upper
859 oceanic crust: A study of seawater-basalt exchange at ODP Sites 504B and 896A. *Earth Planet. Sci.*
860 *Lett.* **201**, 187–201.
- 861 Chan L. H., Edmond J. M., Thompson G. and Gillis K. (1992) Lithium isotopic composition of submarine
862 basalts: implications for the lithium cycle in the oceans. *Earth Planet. Sci. Lett.* **108**, 151–160.
- 863 Chan L. H. and Kastner M. (2000) Lithium isotopic compositions of pore fluids and sediments in the Costa
864 Rica subduction zone: Implications for fluid processes and sediment contribution to the arc
865 volcanoes. *Earth Planet. Sci. Lett.* **183**, 275–290.
- 866 Chanda P. and Fantle M. S. (2017) Quantifying the effect of diagenetic recrystallization on the Mg
867 isotopic composition of marine carbonates. *Geochim. Cosmochim. Acta* **204**, 219–239.
- 868 Delaney M. L. and Linn L. J. (1993) 33 . Interstitial Water and Bulk Calcite Chemistry, Leg 130, and Calcite
869 Recrystallization. *Proc. Ocean Drill. Progr.* **130**, 561–572.
- 870 Dellinger M., Bouchez J., Gaillardet J., Faure L. and Moureau J. (2017) Tracing weathering regimes using
871 the lithium isotope composition of detrital sediments. *Geology* **45**, 411–414.
- 872 Dellinger M., Gaillardet J., Bouchez J., Calmels D., Galy V., Hilton R. G., Louvat P. and France-Lanord C.
873 (2014) Lithium isotopes in large rivers reveal the cannibalistic nature of modern continental
874 weathering and erosion. *Earth Planet. Sci. Lett.* **401**, 359–372.
- 875 Dellinger M., Hardisty D. S., Planavsky N. J., Gill B. C., Kalderon-Asael B., Asael D., Croissant T., Swart P. K.
876 and West A. J. (2020) The effects of diagenesis on lithium isotope ratios of shallow marine
877 carbonates. *Am. J. Sci.* **320**, 150–184.
- 878 Dellinger M., Joshua West A., Paris G., Adkins J. F., Pogge von Strandmann P., Ullmann C. V., Eagle R. A.,
879 Freitas P., Bagard M.-L., Ries J. B., Corsetti F. A., Perez-Huerta A. and Kampf A. R. (2018) The Li
880 isotope composition of marine biogenic carbonates: Patterns and Mechanisms. *Geochim.*
881 *Cosmochim. Acta* **236**, 315–335.
- 882 Druhan J. L. and Maher K. (2014) A Model Linking Stable Isotope Fractionation to Water Flux and Transit
883 Times in Heterogeneous Porous Media. *Procedia Earth Planet. Sci.* **10**, 179–188.
- 884 Fantle M. S. (2015) Calcium isotopic evidence for rapid recrystallization of bulk marine carbonates and
885 implications for geochemical proxies. *Geochim. Cosmochim. Acta* **148**, 378–401.
- 886 Fantle M. S., Barnes B. D. and Lau K. V. (2020) The Role of Diagenesis in Shaping the Geochemistry of the

- 887 Marine Carbonate Record. *Annu. Rev. Earth Planet. Sci.* **48**, 549–583.
- 888 Fantle M. S. and DePaolo D. J. (2007) Ca isotopes in carbonate sediment and pore fluid from ODP Site
889 807A: The Ca²⁺(aq)-calcite equilibrium fractionation factor and calcite recrystallization rates in
890 Pleistocene sediments. *Geochim. Cosmochim. Acta* **71**, 2524–2546.
- 891 Fantle M. S. and DePaolo D. J. (2006) Sr isotopes and pore fluid chemistry in carbonate sediment of the
892 Ontong Java Plateau: Calcite recrystallization rates and evidence for a rapid rise in seawater Mg
893 over the last 10 million years. *Geochim. Cosmochim. Acta* **70**, 3883–3904.
- 894 Fantle M. S. and Higgins J. (2014) The effects of diagenesis and dolomitization on Ca and Mg isotopes in
895 marine platform carbonates: Implications for the geochemical cycles of Ca and Mg. *Geochim.*
896 *Cosmochim. Acta* **142**, 458–481.
- 897 Fantle M. S., Maher K. M. and DePaolo D. J. (2010) Isotopic approaches for quantifying the rates of
898 marine burial diagenesis. *Rev. Geophys.* **48**, 1–38.
- 899 Fernandez N. M., Zhang X. and Druhan J. L. (2019) Silicon isotopic re-equilibration during amorphous
900 silica precipitation and implications for isotopic signatures in geochemical proxies. *Geochim.*
901 *Cosmochim. Acta* **262**, 104–127.
- 902 Geilert S., Vroon P. Z., Roerdink D. L., Van Cappellen P. and van Bergen M. J. (2014) Silicon isotope
903 fractionation during abiotic silica precipitation at low temperatures: Inferences from flow-through
904 experiments. *Geochim. Cosmochim. Acta* **142**, 95–114.
- 905 Gorski C. A. and Fantle M. S. (2017) Stable mineral recrystallization in low temperature aqueous
906 systems: A critical review. *Geochim. Cosmochim. Acta* **198**, 439–465.
- 907 Hall J. M., Chan L. H., McDonough W. F. and Turekian K. K. (2005) Determination of the lithium isotopic
908 composition of planktic foraminifera and its application as a paleo-seawater proxy. *Mar. Geol.* **217**,
909 255–265.
- 910 Hathorne E. C. and James R. H. (2006) Temporal record of lithium in seawater: A tracer for silicate
911 weathering? *Earth Planet. Sci. Lett.* **246**, 393–406.
- 912 Hein J. R., Yeh H. W. and Alexander E. (1979) Origin of iron-rich montmorillonite from the manganese
913 nodule belt of the North Equatorial Pacific. *Clays Clay Miner.* **27**, 185–194.
- 914 Hindshaw R. S., Tosca R., Goût T. L., Farnan I., Tosca N. J. and Tipper E. T. (2019) Experimental
915 constraints on Li isotope fractionation during clay formation. *Geochim. Cosmochim. Acta* **250**, 219–
916 237.
- 917 Hoefs J. and Sywall M. (1997) Lithium isotope composition of Quaternary and Tertiary biogene
918 carbonates and a global lithium isotope balance. *Geochim. Cosmochim. Acta* **61**, 2679–2690.
- 919 Huber C., Druhan J. L. and Fantle M. S. (2017) Perspectives on geochemical proxies: The impact of model
920 and parameter selection on the quantification of carbonate recrystallization rates. *Geochim.*
921 *Cosmochim. Acta* **217**, 171–192.
- 922 Huh Y., Chan L. H., Zhang L. and Edmond J. M. (1998) Lithium and its isotopes in major world rivers:
923 implications for weathering and the oceanic budget. *Geochim. Cosmochim. Acta* **62**, 2039–2051.
- 924 Kisakurek B., James R. H. and Harris N. B. W. (2005) Li and $\delta^7\text{Li}$ in Himalayan rivers: Proxies for silicate
925 weathering? *Earth Planet. Sci. Lett.* **237**, 387–401.

- 926 Lechler M., Pogge von Strandmann P. A. E., Jenkyns H. C., Prosser G. and Parente M. (2015) Lithium-
 927 isotope evidence for enhanced silicate weathering during OAE 1a (Early Aptian Selli event). *Earth*
 928 *Planet. Sci. Lett.* **432**, 210–222.
- 929 Li G. and West A. J. (2014) Evolution of Cenozoic seawater lithium isotopes: Coupling of global
 930 denudation regime and shifting seawater sinks. *Earth Planet. Sci. Lett.* **401**, 284–293.
- 931 Magna T., Wiechert U. H. and Halliday A. N. (2004) Low-blank isotope ratio measurement of small
 932 samples of lithium using multiple-collector ICPMS. *Int. J. Mass Spectrom.* **239**, 67–76.
- 933 Marriott C. S., Henderson G. M., Belshaw N. S. and Tudhope A. W. (2004a) Temperature dependence of
 934 $\delta^7\text{Li}$, $\delta^{44}\text{Ca}$ and Li/Ca during growth of calcium carbonate. *Earth Planet. Sci. Lett.* **222**, 615–624.
- 935 Marriott C. S., Henderson G. M., Crompton R., Staubwasser M. and Shaw S. (2004b) Effect of mineralogy,
 936 salinity, and temperature on Li/Ca and Li isotope composition of calcium carbonate. *Chem. Geol.*
 937 **212**, 5–15.
- 938 Martin J. B., Kastner M. and Elderfield H. (1991) Lithium: sources in pore fluids of Peru slope sediments
 939 and implications for oceanic fluxes. *Mar. Geol.* **102**, 281–292.
- 940 Michalopoulos P. and Aller R. (1995) Rapid Clay Mineral Formation in Amazon Delta Sediments: Reverse
 941 Weathering and Oceanic Elemental Cycles. *Science (80-.)*. **270**, 614–617.
- 942 Michalopoulos P. and Aller R. C. (2004) Early diagenesis of biogenic silica in the Amazon delta:
 943 Alteration, authigenic clay formation, and storage. *Geochim. Cosmochim. Acta* **68**, 1061–1085.
- 944 Michalopoulos P., Aller R. C. and Reeder R. J. (2000) Conversion of diatoms to clays during early
 945 diagenesis in tropical, continental shell muds. *Geology* **28**, 1095–1098.
- 946 Millot R., Vigier N. and Gaillardet J. (2010) Behaviour of lithium and its isotopes during weathering in the
 947 Mackenzie Basin, Canada. *Geochim. Cosmochim. Acta* **74**, 3897–3912.
- 948 Misra S. and Froelich P. N. (2012) Lithium Isotope History of Cenozoic Seawater: Changes in Silicate
 949 Weathering and Reverse Weathering. *Science (80-.)*. **335**, 818–823.
- 950 Palike H., Lyle M., Raffi I. and Klaus A. (2010a) Methods. *Proc. IODP* **320**.
- 951 Palike H., Lyle M., Raffi I. and Klaus A. (2010b) Site U1338 Report. *Proc. IODP* **320**.
- 952 Pistiner J. S. and Henderson G. M. (2003) Lithium-isotope fractionation during continental weathering
 953 processes. *Earth Planet. Sci. Lett.* **214**, 327–339.
- 954 Pogge von Strandmann P. A. E., Desrochers A., Murphy M. J., Finlay A. J., Selby D. and Lenton T. M. (2017)
 955 Global climate stabilisation by chemical weathering during the Hirnantian glaciation. *Geochemical*
 956 *Perspect. Lett.* **3**, 230–237.
- 957 Pogge von Strandmann P. A. E., Elliott T., Marschall H. R., Coath C., Lai Y.-J., Jeffcoate A. B. and Ionov D.
 958 A. (2011) Variations of Li and Mg isotope ratios in bulk chondrites and mantle xenoliths. *Geochim.*
 959 *Cosmochim. Acta* **75**, 5247–5268.
- 960 Pogge von Strandmann P. A. E., Fraser W. T., Hammond S. J., Tarbuck G., Wood I. G., Oelkers E. H. and
 961 Murphy M. J. (2019a) Experimental determination of Li isotope behaviour during basalt
 962 weathering. *Chem. Geol.* **517**, 34–43.
- 963 Pogge von Strandmann P. A. E., James R. H., van Calsteren P., Gíslason S. R. and Burton K. W. (2008)

- 964 Lithium, magnesium and uranium isotope behaviour in the estuarine environment of basaltic
965 islands. *Earth Planet. Sci. Lett.* **274**, 462–471.
- 966 Pogge von Strandmann P. A. E., Jenkyns H. C. and Woodfine R. G. (2013) Lithium isotope evidence for
967 enhanced weathering during Oceanic Anoxic Event 2. *Nat. Geosci.* **6**, 668–672.
- 968 Pogge von Strandmann P. A. E., Schmidt D. N., Planavsky N. J., Wei G., Todd C. L. and Baumann K. H.
969 (2019b) Assessing bulk carbonates as archives for seawater Li isotope ratios. *Chem. Geol.* **530**,
970 119338.
- 971 Richter F. M. and DePaolo D. J. (1987) Numerical models for diagenesis and the Neogene Sr isotopic
972 evolution of seawater from DSDP Site 590B. *Earth Planet. Sci. Lett.* **83**, 27–38.
- 973 Richter F. M., Mendybaev R. a., Christensen J. N., Hutcheon I. D., Williams R. W., Sturchio N. C. and
974 Beloso A. D. (2006) Kinetic isotopic fractionation during diffusion of ionic species in water.
975 *Geochim. Cosmochim. Acta* **70**, 277–289.
- 976 Roerdink D. L., van den Boorn S. H. J. M., Geilert S., Vroon P. Z. and van Bergen M. J. (2015) Experimental
977 constraints on kinetic and equilibrium silicon isotope fractionation during the formation of non-
978 biogenic chert deposits. *Chem. Geol.* **402**, 40–51.
- 979 Rudnick R. L., Tomascak P. B., Njo H. B. and Gardner L. R. (2004) Extreme lithium isotopic fractionation
980 during continental weathering revealed in saprolites from South Carolina. *Chem. Geol.* **212**, 45–57.
- 981 Schrag D. P., DePaolo D. J. and Richter F. M. (1992) Oxygen Isotope Exchange in a 2-Layer Model of
982 Oceanic-Crust. *Earth Planet. Sci. Lett.* **111**, 305–317.
- 983 Spinelli G. A., Giambolvo E. R. and Fisher A. T. (2004) Sediment permeability, distribution, and influence
984 on fluxes in oceanic basement. In *Hydrogeology of the Oceanic Lithosphere* (eds. E. E. Davis and H.
985 Elderfield). Cambridge University Press. pp. 151–188.
- 986 Steefel C. I., Appelo C. A. J., Arora B., Jacques D., Kalbacher T., Kolditz O., Lagneau V., Lichtner P. C.,
987 Mayer K. U., Meeussen J. C. L., Molins S., Moulton D., Shao H., Šimůnek J., Spycher N., Yabusaki S.
988 B. and Yeh G. T. (2015) *Reactive transport codes for subsurface environmental simulation.*,
- 989 Steefel C. I., Druhan J. L. and Maher K. (2014) Modeling Coupled Chemical and Isotopic Equilibration
990 Rates. *Procedia Earth Planet. Sci.* **10**, 208–217.
- 991 Stoffyn-Egli P. and Mackenzie F. T. (1984) Mass balance of dissolved lithium in the oceans. *Geochim.*
992 *Cosmochim. Acta* **48**, 859–872.
- 993 Tomascak P. B., Magna T. and Dohmen R. (2016) *Advances in Lithium Isotope Geochemistry.*, Springer.
- 994 Ullmann C. V, Campbell H. J., Frei R., Hesselbo S. P., Pogge von Strandmann P. A. E. and Korte C. (2013)
995 Partial diagenetic overprint of Late Jurassic belemnites from New Zealand: Implications for the
996 preservation potential of $\delta^7\text{Li}$ values in calcite fossils. *Geochim. Cosmochim. Acta* **120**, 80–96.
- 997 Verney-Carron A., Vigier N. and Millot R. (2011) Experimental determination of the role of diffusion on Li
998 isotope fractionation during basaltic glass weathering. *Geochim. Cosmochim. Acta* **75**, 3452–3468.
- 999 Vigier N., Decarreau A., Millot R., Carignan J., Petit S. and France-Lanord C. (2008) Quantifying Li isotope
1000 fractionation during smectite formation and implications for the Li cycle. *Geochim. Cosmochim.*
1001 *Acta* **72**, 780–792.

- 1002 Vigier N., Rollion-Bard C., Spezzaferri S. and Brunet F. (2007) In situ measurements of Li isotopes in
1003 foraminifera. *Geochemistry, Geophys. Geosystems* **8**.
- 1004 Voigt J., Hathorne E. C., Frank M., Vollstaedt H. and Eisenhauer A. (2015) Variability of carbonate
1005 diagenesis in equatorial Pacific sediments deduced from radiogenic and stable Sr isotopes.
1006 *Geochim. Cosmochim. Acta* **148**, 360–377.
- 1007 Wimpenny J., Colla C. A., Yu P., Yin Q. Z., Rustad J. R. and Casey W. H. (2015) Lithium isotope
1008 fractionation during uptake by gibbsite. *Geochim. Cosmochim. Acta* **168**, 133–150.
- 1009 You C. F., Chan L. H., Gieskes J. M. and Klinkhammer G. P. (2003) Seawater intrusion through the oceanic
1010 crust and carbonate sediment in the Equatorial Pacific: Lithium abundance and isotopic evidence.
1011 *Geophys. Res. Lett.* **30**, 2120.
- 1012 You C. F., Chan L. H., Spivack A. J. and Gieskes J. M. (1995) Lithium, boron, and their isotopes in
1013 sediments and pore waters of Ocean Drilling Program site 808, Nankai Trough: implications for
1014 fluid expulsion in accretionary prisms. *Geology* **23**, 37–40.
- 1015 Zhang L., Chan L. H. and Gieskes J. M. (1998) Lithium isotope geochemistry of pore waters from Ocean
1016 Drilling Program Sites 918/919, Irminger Basin. *Geochim. Cosmochim. Acta* **62**, 2437–2450.
- 1017
- 1018

1019

1020 **Figure Captions**

1021

1022 Figure 1. (a) Location of IODP Expedition 320/321 drill sites. Map courtesy of IODP-JRSO. (b)
 1023 Stratigraphic column and lithologic unit, (c) porosity of the section, (d) weight percent CaCO_3 in
 1024 sediment, (e) weight percent SiO_2 in sediment, (f) age-depth profile for the section, and (g)
 1025 temperature-depth profile for Site U1338A. Data from Palike et al. (2010b)

1026

1027 Figure 2. Pore fluid chemistry of Site U1338A. (a) Li concentration, (b) Sr concentration, (c)
 1028 H_4SiO_4 concentration, (d) pH, (e) Mg concentration, (f) Ca concentration, (g) sulfate
 1029 concentration, and (h) alkalinity. Simple unit descriptions and boundaries are added for clarity.
 1030 Data from Palike et al., (2010b).

1031

1032 Figure 3. Lithium isotopic composition of pore fluids, exchangeable fraction, carbonate fraction
 1033 and residual silicate fraction at Site U1338A. The error bars represent 1 standard deviation. The
 1034 vertical line represents the isotopic composition of modern seawater and the horizontal lines
 1035 represent unit boundaries.

1036

1037 Figure 4. Concentration of Li in pore fluids and the concentration in each of the fractions of the
 1038 sequential sediment leach (presented as ng Li/cm^3 porous media). (a) pore fluid concentration
 1039 from Palike et al., (2010b) for reference, (b) Li concentration in the exchangeable fraction, (c) Li
 1040 concentration in the carbonate fraction, and (d) Li concentration in the residual fraction. Dashed
 1041 lines denote the unit boundaries.

1042

1043 Figure 5. SEM images of sediment and XRD data. (a) SEM image of well-preserved diatom
 1044 from ~146 rmc (b) SEM image of coated diatoms from ~44 rmc. (c) EDS data overlaying
 1045 SEM image from 5a. (d) EDS data overlaying SEM image from 5b. (e) X-ray diffraction (XRD)
 1046 data from Site 1338 samples 1-H-1, 15-H-3, 38-X-3, and 44-X-2 presented as a function of 2θ
 1047 and (f) d-spacing. The calcite peaks were picked using the Jade software package, and the
 1048 smectite peaks identified using literature values (Chipera and Bish, 2001).

1049

1050 Figure 6. Reactive transport simulations of the burial of Unit III over 10.6 Ma at Site U1338
 1051 assuming two scenarios: (a-b) a change in authigenic clay reactivity between Units I/II and Unit
 1052 III and its impact on (a) pore fluid Li concentration and (b) $\delta^7\text{Li}$ of pore fluid and authigenic
 1053 solid; (c-d) a change in the fractionation factor associated with authigenic clay precipitation in
 1054 Unit III and its impact on (a) pore fluid Li concentration and (b) $\delta^7\text{Li}$ of pore fluid and authigenic
 1055 solid. In (d), the thicker black curves refer to authigenic clay formed in Units I/II and the gray
 1056 curves refer to the authigenic clay formed in Unit III. In (a-b), the term 'reactivity' refers
 1057 specifically to a 20x difference in specific surface area (m^2/g) between authigenic clay in Unit III
 1058 and authigenic clay in Units I/II; the intrinsic rate constants associated with authigenic clay
 1059 precipitation are the same for both units, as are the fractionation factors associated with
 1060 authigenesis ($\alpha_{\text{clay} - \text{fluid}}$). Because precipitation rate is a function of surface area, the intrinsic
 1061 rate constant, and the saturation state, the 20x difference in surface area does not necessarily
 1062 correlate with a 20x different in precipitation rate. Precipitation rates in the 20x scenario are
 1063 generally no more than twice those in the 'equal reactivity' scenario (i.e., equal specific surface
 1064 area).

1065
 1066 Figure 7. Compilation of pore fluid Li concentration gradients in the modern ocean at a range of
 1067 ODP and IODP sites. (a) Map summary of sites that have positive (red), negative (green), or
 1068 hybrid (yellow) gradients over the upper 50-100 meters of the section. Examples of sites that
 1069 have (b) decreasing/negative, (c) increasing/positive, and (d) hybrid Li concentration profiles
 1070 with depth. The latter typically exhibit sink profiles over ~50-100 meters at the top of the
 1071 section, but increase below this depth to Li concentrations that are usually greater than the
 1072 modern seawater Li concentration (i.e., 26 μM). Also noted in the lowermost row of panels is the
 1073 CaCO_3 content of each site as a function of depth.

1074
 1075 Figure 8. Generic reactive transport model simulations of pore fluid Li concentration and
 1076 isotopic composition for two cases: (i) continuous and (ii) discrete deposition and burial of
 1077 reactive silica. Case (i) simulations are shown in panels (a-d), while Case (ii) simulations are
 1078 shown in panels (e-h). In each row, from left to right, the parameters depicted are: pore fluid Li^+
 1079 concentration, pore fluid $\text{SiO}_2(\text{aq})$ concentration, authigenic solid Li concentration, and pore
 1080 fluid and authigenic solid $\delta^7\text{Li}$.

1081
 1082 Figure 9. Calculated $\delta^7\text{Li}$ of diffusive flux of Li out of the ocean, as a function of the diffusive
 1083 mass flux, for the (a) continuous and (b) discrete deposition and burial scenarios described in
 1084 Fig. 8. The diffusive mass flux is a maximum estimate determined assuming authigenesis occurs
 1085 over a surface area of $3 \cdot 10^8 \text{ km}^2$ (deep-sea only, no continental shelves; e.g., Turcotte and
 1086 Schubert, 1982)

1087
 1088 Figure 10. Model output from depositional reactive transport model (e.g., Fantle and DePaolo,
 1089 2006). For the carbonate recrystallization-only scenario, the modeled (green, yellow, blue, and
 1090 pink curves) and measured (\circ) (a) pore fluid Li concentrations (μM), (b) pore fluid $\delta^7\text{Li}$ values
 1091 (‰), bulk carbonate Li concentrations ($\mu\text{mol/kg}$) when the initial Li concentration is (c) 1
 1092 $\mu\text{mol/kg}$ or (d) 30 $\mu\text{mol/kg}$, and bulk carbonate $\delta^7\text{Li}$ values (‰) when the initial Li concentration
 1093 is (e) 1 $\mu\text{mol/kg}$, or (f) 30 $\mu\text{mol/kg}$. In panels (a) through (f), the partition coefficient for Li in the
 1094 bulk carbonate (K_{Li}) is varied from $3 \cdot 10^{-3}$ to $3 \cdot 10^{-2}$, as indicated in (a), (c), and (d). Model output
 1095 for the carbonate recrystallization + authigenic clay precipitation scenario, in which all model
 1096 parameters are the same as the simulations above ($K_{\text{Li}}=3 \cdot 10^{-3}$), except that the pore fluid $\delta^7\text{Li}$
 1097 values and pore fluid Li concentrations as functions of depth and time are constrained as
 1098 described in the text. The (g) $\delta^7\text{Li}$ (‰) and (h) bulk carbonate Li concentration ($\mu\text{mol/kg}$) output
 1099 for the scenario shown is one in which the pore fluid Li (i) concentration and (j) isotopic
 1100 composition varies over time within (k) a 25-m reactive layer that is deposited at 125 m above
 1101 basement. In all simulations, the initial pore fluid and bulk carbonate $\delta^7\text{Li}$ is assumed to be that
 1102 inferred for seawater by Misra and Froelich (2012) over the depositional time scale appropriate
 1103 to Site 1338. The bulk carbonate recrystallization rate (R) utilized in all the models shown in this
 1104 figure is a function of sediment age (e.g., Fantle and DePaolo, 2006) and is constrained by our
 1105 modeling of Sr geochemistry at Site 1338 ($R[\text{Ma}^{-1}] = 0.07 \cdot e^{-\text{age}/5.25}$; Fig. S3).

1106
 1107 Figure 11. (a) Bulk carbonate isotopic composition of samples from Site U1338A plotted with
 1108 bulk carbonate isotopic composition of samples from Site 851B (You et al., 2003). (b) Bulk
 1109 carbonate isotopic composition of samples from Site U1338A plotted as a function of age

1110 alongside foraminiferal $\delta^7\text{Li}$ measured over the past 70 Ma (Misra and Froelich, 2012; James and
1111 Hathorne, 2006).
1112
1113

Journal Pre-proofs

1114 **Tables**

1115

1116 *Table 1. Mass balance constraints on the proportion of clay in the 1338 sedimentary section.*

Sample	Depth (rmcd)	m_{Li}^{HF} (ppm) ^a	Authigenic Clay		Detrital Clay	
			% clay ^b	% SiO ₂ (bio) ^c	% clay ^b	% SiO ₂ (bio) ^c
1-H-1 142-144	1.49	3.45	0.29	99.71	3.01	96.99
5-H-5 143-145	44.05	21.08	3.83	96.17	39.75	60.25
7-H-3 143-145	60.86	16.44	2.90	97.10	30.08	69.92
9-H-3 140-142	83.1	2.11	0.02	99.98	0.24	99.76
15-H-3 144-146	146.5	4.64	0.53	99.47	5.49	94.51
21-H-3 144-146	210.14	5.98	0.80	99.20	8.29	91.71
23-H-3 143-145	231.84	7.17	1.04	98.96	10.78	89.22
26-H-3 144-146	263.43	9.74	1.55	98.45	16.13	83.87
32-X-3 138-140	325.57	4.10	0.42	99.58	4.37	95.63
34-X-3 138-140	347.53	8.54	1.31	98.69	13.63	86.37
38-X-3 138-140	380.93	20.01	3.62	96.38	37.53	62.47
44-X-2 139-141	451.56	8.82	1.37	98.63	14.20	85.80

1117 a – Concentration of Li in the HF-soluble fraction of the bulk sediment.

1118 b – Percentage of clay and biogenic silica required to fit the measured Li concentration in the residual fraction.

1119 Mixing calculation assumed Li concentrations of 500 ppm for authigenic clay (Hein et al., 1979), 50 ppm detrital
1120 clay (Zhang et al., 1998), and 2 for biogenic silica (Chan and Kastner, 2000).

1121 c – Biogenic silica, such as diatoms and radiolaria.

1122

1123

1124